1 # Augmentation and Use of WRF-Hydro to Simulate Overland Flow-
2 # and Streamflow-Generated Debris Flow Hazards in Burn Scars

4 **Chuxuan Li[1], Alexander L. Handwerger[2,3], Jiali Wang[4], Wei Yu[5,6], Xiang Li[7], Noah J.**
5 **Finnegan[8], Yingying Xie[9,10], Giuseppe Buscarnera[7], and Daniel E. Horton[1]**

6 [1] Department of Earth and Planetary Sciences, Northwestern University, Evanston, IL, 60208, USA

7 [2] Joint Institute for Regional Earth System Science and Engineering, University of California, Los Angeles,
8 CA, 90095, USA

9 [3] Jet Propulsion Laboratory, California Institute of Technology, Pasadena, CA, 91109, USA

10 [4] Environmental Science Division, Argonne National Laboratory, Lemont, IL, 60439, USA

11 [5] Cooperative Institute for Research in Environmental Sciences, University of Colorado Boulder, CO,
12 80309, USA

13 [6] NOAA/Global Systems Laboratory, 325 Broadway Boulder, Denver, CO, 80305-3328, USA

14 [7] Department of Civil and Environmental Engineering, Northwestern University, Evanston, IL, 60208, USA

15 [8] University of California Santa Cruz, Department of Earth and Planetary Sciences, Santa Cruz, CA, 95064,
16 USA

17 [9] Program in Environmental Sciences, Northwestern University, 2145 Sheridan Road, Evanston, IL, 60208,
18 USA

19 [10] Department of Biological Sciences, Purdue University, 915 W State St, West Lafayette, IN 47907, USA

21 *Correspondence to:* Chuxuan Li (chuxuanli2020@u.northwestern.edu)

31 **Abstract**

32 In steep wildfire-burned terrains, intense rainfall can produce large volumes of runoff that can
33 trigger highly destructive debris flows. The ability to accurately characterize and forecast debris-
34 flow hazards in burned terrains, however, remains limited. Here, we augment the Weather
35 Research and Forecasting Hydrological modeling system (WRF-Hydro) to simulate both overland
36 and channelized flows and assess postfire debris-flow hazards over a regional domain. We perform
37 hindcast simulations using high-resolution weather radar-derived precipitation and reanalysis data
38 to drive non-burned baseline and burn scar sensitivity experiments. Our simulations focus on
39 January 2021 when an atmospheric river triggered numerous debris flows within a wildfire burn
40 scar in Big Sur – one of which destroyed California's famous Highway 1. Compared to the
41 baseline, our burn scar simulation yields dramatic increases in total and peak discharge, and shorter
42 lags between rainfall onset and peak discharge. At Rat Creek, where Highway 1 was destroyed,
43 discharge volume increases eight-fold and peak discharge triples relative to the baseline. For all
44 catchments within the burn scar, we find that the median catchment-area normalized discharge
45 volume increases nine-fold after incorporating burn scar characteristics, while the 95th percentile
46 volume increases 13-fold. Catchments with anomalously high hazard levels correspond well with
47 post-event debris flow observations. Our results demonstrate that WRF-Hydro provides a
48 compelling new physics-based tool to investigate and potentially forecast postfire hydrologic
49 hazards at regional scales.

50

51 **Short Summary**

52 In January 2021 a storm triggered numerous debris flows in a wildfire burn scar in California. We
53 use a hydrologic model to assess debris flow hazards in pre-fire and postfire scenarios. Compared
54 to pre-fire conditions, the postfire simulation yields dramatic increases in total and peak discharge,
55 substantially increasing debris flow hazards. Our work demonstrates the utility of 3-D hydrologic
56 models for investigating and potentially forecasting postfire debris flow hazards at regional
57 scales.

58

59 **1 Introduction**

60 Following intense rainfall, areas with wildfire burn scars are more prone to flash flooding (Neary
61 et al., 2003; Bart & Hope 2010; Bart 2016) and runoff-generated debris flow hazards than
62 unburned areas (Moody et al., 2013; Ice et al., 2004; Shakesby & Doerr, 2006). After wildfire,
63 reduced tree canopy interception, decreased soil infiltration due to soil-sealing effects (Larsen et
64 al., 2009), and increased soil water repellency – especially in hyper-arid environments (Dekker
65 and Ritsema, 1994; Doerr and Thomas, 2000; MacDonald and Huffman, 2004) – increases excess
66 surface water, and on sloped terrains leads to overland flow (Shakesby & Doerr, 2006; Stoof et al.,

2012). As water moves down hillslopes and erosion adds sediment to water-dominated flows, clear water floods can transition to turbulent and potentially destructive debris flows (Meyer & Wells, 1997; Cannon et al., 2001, 2003; Santi et al., 2008). In contrast to debris flows initiated by shallow landslides, this rainfall-runoff process has been identified as the major cause for postfire debris flows in the western U.S. (Cannon, 2001; Cannon et al., 2003, 2008; Kean et al., 2011; Nyman et al., 2015; Parise & Cannon, 2012), and in other regions with Mediterranean climates (Mitsopoulos & Mironidis, 2006; Bisson et al., 2005; Parise & Cannon, 2008, 2009; Rosso et al., 2007). In California, because climate change is projected to increase the intensity and frequency of wet-season precipitation (Swain et al., 2018; Polade et al., 2017), increase wildfire potential (Swain, 2021; Brown et al., 2021), and extend the wildfire season (Goss et al., 2020), occurrence and intensity of postfire debris flows are likely to increase (Cannon et al., 2009; Kean & Staley, 2021; Oakley, 2021).

To assess postfire debris flow hazards, statistical approaches including empirical models and machine-learning techniques are commonly used in both research and operational settings (Gardner et al., 2014; Cannon et al., 2010; Staley et al., 2016; Cui et al., 2019; Nikolopoulos et al., 2018; Friedel 2011a, 2011b). Statistical approaches are useful for identifying and characterizing relationships amongst contributing environmental factors and are helpful in operational settings due to low computational costs and the potential for rapid assessment. For example, the U.S. Geological Survey (USGS) currently employs a statistical approach in their Emergency Assessment of Postfire Debris-flow Hazards that consists of a logistic regression model to predict the likelihood of post-wildfire debris flows (e.g., Staley et al., 2016; Cannon et al., 2010), and a multiple linear regression model to predict debris flow volumes (Gartner et al., 2014). Machine-learning techniques have also been used to predict postfire debris flows in the western U.S. (Nikolopoulos et al., 2018; Friedel 2011a, 2011b). For example, self-organizing maps and genetic programming were used to predict postfire debris flow occurrence (Friedel 2011b) and volumes (Friedel 2011a), respectively. Compared to the current USGS predictive models, genetic programming was posited to be more useful in solving non-linear multivariate problems (Friedel 2011a), while a random forest algorithm demonstrated increased performance in predicting postfire debris flow occurrence (Nikolopoulos et al., 2018). Despite the utility and advantages of data-driven hazard prediction approaches, these techniques do not simulate the underlying physics, which limits their utility in developing a better process-based understanding of debris flow mechanics, limits their applicability in climatological and geographic settings different than their training sites, and limits their use in non-stationary conditions (e.g., under changing climatic conditions).

In contrast, physics-based models that simulate spatially-explicit hydrologic and mass wastage processes are well-suited for mechanistic sensitivity analyses in diverse settings, but applications of these models have tended to focus on landslide-induced debris flows (e.g., Iverson & George, 2014; George & Iverson, 2014), rather than runoff-generated debris flows which are more common in postfire areas (Cannon et al., 2001, 2003; Santi et al., 2008). Studies that have investigated postfire hydrologic responses using process-based models have largely focused on short-term

107   responses in individual catchments at high spatiotemporal resolutions (McGuire et al., 2016, 2017;
108   Rengers et al., 2016) or long-term runoff responses at coarse temporal resolutions (Rulli & Rosso,
109   2007; McMichael & Hope, 2007). For example, process-based models have employed shallow
110   water equations to understand the triggering and transport mechanisms of postfire debris flows in
111   single catchments (McGuire et al., 2016, 2017) and to investigate the timing of postfire debris
112   flows in three separate catchments (Rengers et al., 2016), the latter of which also assessed the
113   efficacy of a simplified kinematic wave approach. In addition to individual catchment applications,
114   process-based models often adopt simplifications that can limit effective prediction and hypothesis
115   testing to overcome computational limits. For example, the kinematic runoff and erosion model
116   (KINEROS2) simplifies drainage basins into 1-dimensional channels and hillslope patches
117   (Canfield & Goodrich, 2005; Goodrich et al., 2012; Sidman et al., 2015), and the Hydrologic
118   Modeling System (HEC-HMS) uses an empirically-based curve number method to estimate
119   saturation excess water (Cydzik et al., 2009), which cannot resolve infiltration excess overland
120   flow, a critical process in burn scars (Chen et al., 2013).

121   Given the current state of debris flow hazard assessment and prediction in previously burned
122   terrains, in addition to the growing influence of anthropogenic climate change on wildfire and
123   extreme precipitation, development of physics-based hazard assessment tools that can be used in
124   both hindcast investigations and forecasting applications is needed. Furthermore, due to the diverse
125   morphology of precipitation events and their interaction with geographically distributed wildfire
126   burn scars, development of tools that can assess hazards over regional domains, particularly in
127   operational forecasting applications, is critical. Here to advance the field of burn scar debris flow
128   hazard assessment, we explore the use of the physics-based and fully-distributed Weather Research
129   and Forecasting Hydrological modeling system version 5.1.1 (WRF-Hydro). WRF-Hydro is an
130   open-source community model developed by the National Center for Atmospheric Research
131   (NCAR). It is the core of National Oceanic and Atmospheric Administration's (NOAA) National
132   Water Model forecasting system, and has been used extensively to study channelized flows (e.g.,
133   Lahmers et al., 2020; Wang et al., 2019). Here, we modify WRF-Hydro to output high temporal
134   resolution fine-scale (100 m) debris flow-relevant overland flow; a process computed using a fully
135   unsteady, explicit, finite difference diffusive wave formulation. Previous efforts, employing
136   shallow water equations, diffusive, kinematic, and diffusive-kinematic wave models, have
137   demonstrated that water-only models can provide critical insights on runoff-driven debris flow
138   behavior (Arattano & Savage, 1994; McGuire & Youberg, 2020; Arratano & Franzi, 2010; Di
139   Cristo et al., 2021), even in burned watersheds (Rengers et al., 2016).

140   To test and demonstrate the utility of WRF-Hydro in debris flow studies, we investigate the
141   January 2021 debris flow events within the Dolan burn scar on the Big Sur coast of central
142   California (Fig. 1a–b). We first identify multiple debris flow sites using optical and radar remote
143   sensing data and field investigations. We then calibrate WRF-Hydro against ground-based soil
144   moisture and streamflow observations and use it to study the effects of burn scars on debris flow
145   hydrology and changes in hazard potential. The paper is organized as follows. Section 2 describes
146   our debris flow identification approach and historical context. Section 3 presents a description of

147 WRF-Hydro. Section 4 describes the simulation, calibration, and validation of WRF-Hydro.
148 Section 5 presents the results. Section 6 discusses the results and Sect. 7 provides a conclusion.
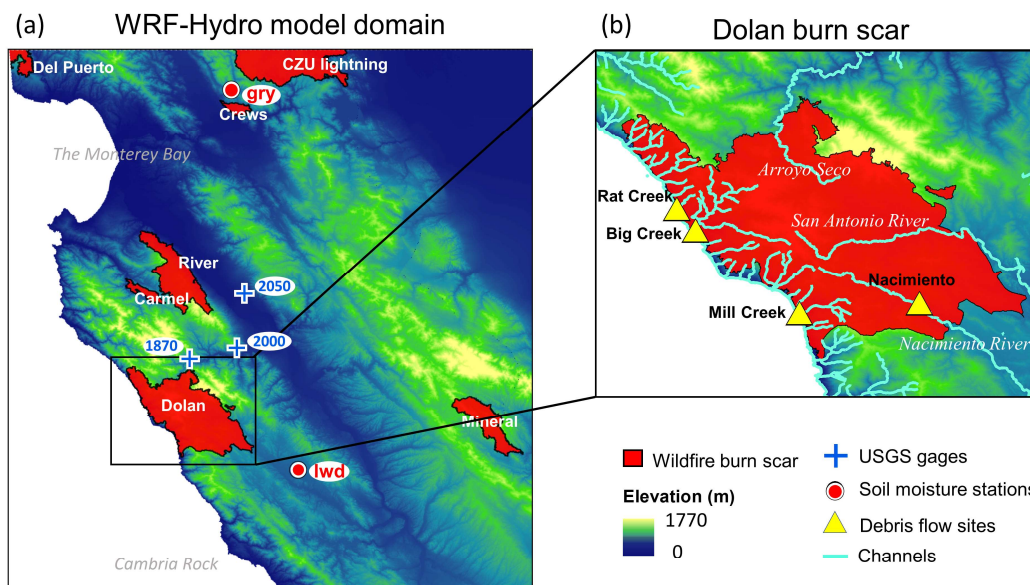
150 **Fig. 1|** WRF-Hydro model domain and Dolan burn scar. (a) WRF-Hydro model domain depicting
151 topography, 2020 wildfire season burn scars, and PSL soil moisture and USGS stream gage
152 observing sites. The black rectangle outlines (b) the Dolan burn scar inset, in which debris flow
153 locations and major streams are marked and labeled.

2 Study domain and debris flow identification methodology

157 The Dolan wildfire burned from August 18th till December 31st, 2020. 55% of areas within the fire
158 perimeter were burned at moderate-to-high severity (Burned Area Emergency Response, 2020).
159 After the fire, USGS Emergency Assessment of Postfire Debris-flow Hazards produced a debris
160 flow hazard assessment using a design storm based statistical model (USGS, 2020). On January
161 27–29, 2021, an atmospheric river (AR) made landfall on the Big Sur coast, bringing more than
162 300 mm of rainfall to California's Coast Ranges (Fig. 2), with a peak rainfall rate of 24 mm h⁻¹.
163 During the AR event, a section of California State Highway 1 (CA1) at Rat Creek was destroyed
164 by a debris flow. CA1 was subsequently closed for three months and rebuilt at a cost of ~$11.5M
165 (Los Angeles Times, 2021).

166
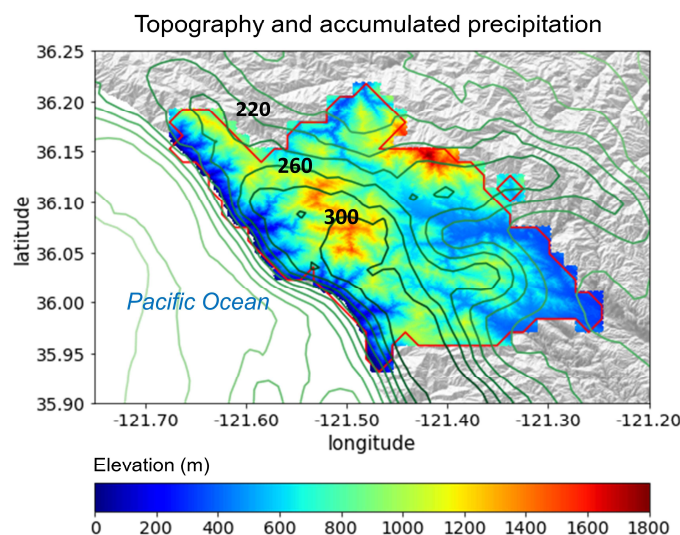
Fig. 2| The topography (shading; m) and MRMS accumulated precipitation (contour lines; mm)
during the AR event from January 27th 00:00 to 29th 23:00 in the Dolan burn scar. Contour line
interval for accumulated precipitation is 20 mm, and lines of 220, 260, and 300 mm are labeled.
The red polygon outlines the perimeter of the Dolan burn scar.

2.1 Debris flow identification from remote sensing and field work

In addition to the Rat Creek debris flow, which made national news (Los Angeles Times, 2021),
we identified three other debris flows using a combination of field investigation, and open access
satellite optical and synthetic aperture radar (SAR) images (Fig. 3 and Fig. B1). We examined
relative differences in normalized difference vegetation index (rdNDVI) defined by (Scheip &
Wegmann, 2021):

$$rdNDVI = \frac{NDVI_{post} - NDVI_{pre}}{\sqrt{NDVI_{pre} + NDVI_{post}}} \times 100 \qquad (1)$$

where $NDVI_{pre}$ and $NDVI_{post}$ are the pre- and post-event normalized difference vegetation index
(NDVI) images computed following:

$$NDVI = \frac{NIR - R}{NIR + Red} \qquad (2)$$

where *NIR* is the near-infrared response and *Red* is the visible red response. rdNDVI was calculated
from Sentinel-2 satellite data using the HazMapper v1.0 Google Earth Engine application (Scheip
& Wegmann, 2021). HazMapper requires selection of an event date, pre-event window (months),

187   post-event window (months), max cloud cover (%) and slope threshold (°). These input
188   requirements filter the number of images used to calculate the rdNDVI. We set the event date to
189   27 January 2021 and used a 3 month pre- and post-event window with 0% max cloud cover and a
190   0° slope threshold to identify vegetation loss associated with the debris flows. We then created a
191   binary map to highlight debris flows (and other vegetation loss) pixels above a rdNDVI vegetation
192   loss threshold. We removed all pixels with rdNDVI > -10.

193   Lastly, we searched for debris flows (and other ground surface deformation) by examining SAR
194   backscatter change with data acquired by the Copernicus Sentinel-1 (S1) satellites (see full
195   description in Handwerger et al., in review). We measured the change in SAR backscatter by using
196   the log ratio approach, defined as

197
$$I_{ratio} = 10 \times log_{10}(\frac{\sigma_{pre}^{0}}{\sigma_{post}^{0}}) \tag{3}$$

198   where σ_{pre}^{0} is a pre-event image stack (defined as the temporal median) of SAR backscatter and
199   σ_{post}^{0} is a post-event image stack. Similar to the HazMapper method, our approach requires
200   selection of an event date, pre-event window (months), post-event window (months) and slope
201   threshold (°). No cloud-cover threshold is needed since SAR penetrates clouds. We used a 3 month
202   pre- and post-event window and 0° slope threshold to identify ground surface changes associated
203   with the debris flows. We then created a binary map to highlight debris flows by removing all
204   pixels with I_{ratio} < 99th percentile value.

205   Identified debris flow source areas and deposition sites were confirmed by field investigation (N.J.
206   Finnegan) and named after the locations where they deposited (i.e., Big Creek, Mill Creek, and
207   Nacimiento). We note that there were likely more debris flows triggered during the AR event.
208   However, given the primary goal of this study – to demonstrate the utility of WRF-Hydro – a
209   comprehensive cataloging of debris flows is beyond this study's scope.
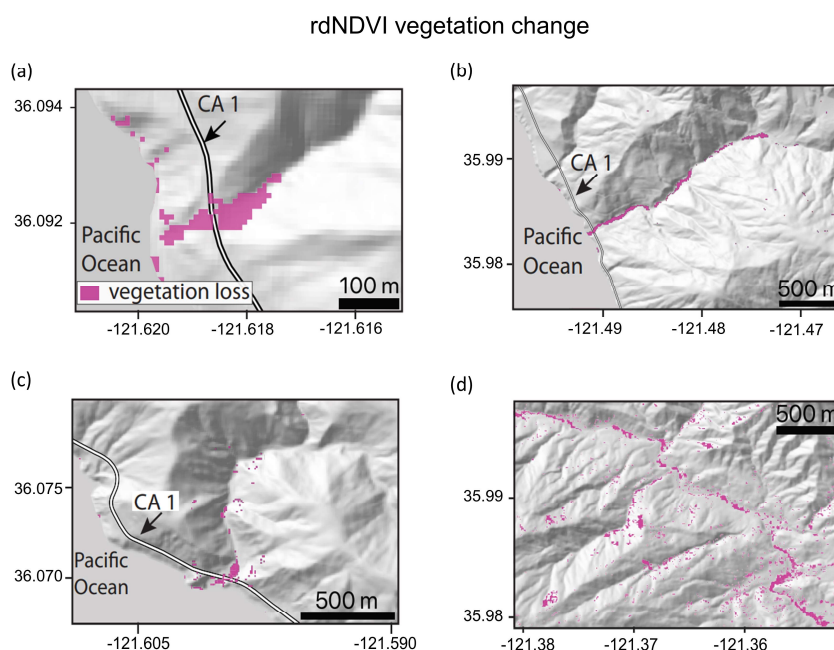
Fig. 3| Identified debris flow sites using rdNDVI vegetation change within the Dolan burn scar. We convert the rdNDVI data into a binary map by setting a threshold value, which yield only the likely debris flow locations. (a)–(d) Sentinel-2 rdNDVI vegetation change at (a) Rat Creek, (b) Mill Creek, (c) Big Creek, and (d) the Nacimiento River.

3 WRF-Hydro

3.1 Model description

WRF-Hydro is an open-source physics-based community model that simulates land surface hydrologic processes. It includes the Noah-Multiparameterization (Noah-MP) land surface model (LSM; Niu et al., 2011), terrain routing module, channel routing module, and a conceptual baseflow bucket model. The Noah-MP LSM is a 1-dimensional column model that calculates vertical energy fluxes (i.e., sensible and latent heat, net radiation), moisture (i.e., canopy interception, infiltration, infiltration excess, deep percolation), and soil thermal and moisture states on the LSM grid (1 km in our application). The infiltration excess, ponded water depth, and soil moisture are then disaggregated using a time-step weighted method (Gochis & Chen, 2003) and sent to the terrain routing module which simulates subsurface and overland flows on a finer terrain routing grid (100 m in our application). According to the mass balance, local infiltration excess,

228 overland flow, and exfiltration from baseflow contribute to the surface head which flows into river
229 channels if defined retention depth is exceeded. The channel routing module then calculates
230 channelized flows assuming a trapezoidal channel shape (Fig. B2). Parameters related to the
231 trapezoidal channel, such as channel bottom width (B_w), Manning's roughness coefficient (n), and
232 channel side slope (z) are functions of channel stream order (Fig. B3 and Table B1). Computed
233 streamflow is then output on the 100 m grid. Equations used to compute infiltration excess,
234 overland flow, and channelized flow are provided in Sect. 3.3 and 3.4.

235 By default, WRF-Hydro uses Moderate Resolution Imaging Spectroradiometer (MODIS)
236 Modified International Geosphere-Biosphere Program (IGBP) 20-category land cover product as
237 land cover (Fig. B4) and 1-km Natural Resources Conservation Service State Soil Geographic
238 (STATSGO) database for soil type classification (Fig. B5; Miller & White, 1998). Land surface
239 properties including canopy height (HVT), maximum carboxylation rate (VCMX25), and overland
240 flow roughness (OV_ROUGH2D) are functions of land cover type (Table B2 & Fig. B4). Default
241 soil hydraulic parameters in WRF-Hydro (i.e., soil porosity, grain size distribution index, and
242 saturated hydraulic conductivity) are based on Cosby et al.'s (1984) soil analysis (Table B3) and
243 are used to map onto the STATSGO 16 soil texture types (Fig. B5).

244

3.2 Meteorological forcing files

245

246 WRF-Hydro is used in standalone mode (i.e., it is not interactively coupled with the atmospheric
247 component of WRF), but rather is forced with a combination of Phase 2 North American Land
248 Data Assimilation System (NLDAS-2) meteorological data and Multi-Radar/Multi-Sensor System
249 (MRMS) radar-only quantitative precipitation (Zhang et al., 2011, 2014, 2016). A description of
250 the MRMS dataset and uncertainties therein can be found in Appendix A. NLDAS-2 provides
251 hourly forcing data including incoming shortwave and longwave radiation, 2-m specific humidity
252 and air temperature, surface pressure, and 10-m wind speed at 1/8-degree spatial resolution.
253 MRMS provides hourly precipitation rate at 1-km resolution.

254

3.3 Overland flow routing and output

255

256 The Noah-MP LSM calculates rate of infiltration excess following Chen & Dudhia (2001):

257

258
$$\frac{\partial h}{\partial t} = \frac{\partial P_d}{\partial t}\left\{1 - \frac{\left[\sum_{i=1}^{4}\Delta D_i(\theta_s-\theta_i)\right]\left[1 - exp\left(-k\frac{K_S}{K_{ref}}\delta_t\right)\right]}{P_d + \left[\sum_{i=1}^{4}\Delta D_i(\theta_s-\theta_i)\right]\left[1 - exp\left(-k\frac{K_S}{K_{ref}}\delta_t\right)\right]}\right\} \tag{4}$$

259

260 where h (m) is the surface water depth and t is the time. P_d (m) is the precipitation not intercepted
261 by the canopy; ΔD_i (m) is the depth of soil layer i; θ_i is the soil moisture in soil layer i; θ_s is the

262   soil porosity; K_s (m s^{-1}) is the saturated hydraulic conductivity; K_{ref} is 2×10^{-6} m s^{-1} which

263   represents the saturated hydraulic conductivity of the silty–clay–loam soil texture chosen as a

264   reference; δ_t (s) is the model time step; and k which is equal to 3.0 is the runoff–infiltration

265   partitioning parameter [the same as kdt_{ref} in Chen & Dudhia (2001)].

266

267   Noah-MP passes excess water to the terrain routing module, which simulates overland flow using

268   a 2-dimensional fully-unsteady, explicit, finite-difference diffusive wave equation adapted from

269   Julien et al. (1995) and Ogden (1997). It is considered superior to the traditionally used kinematic

270   wave formulation in that it accounts for backwater effects and flow over adverse slopes. The

271   diffusive wave formulation is the simplified form of the Saint Venant equations, i.e., continuity

272   and momentum equations for a shallow water wave. The 2-dimensional continuity equation for a

273   flood wave is:

274
$$\frac{\partial h}{\partial t} + \frac{\partial q_x}{\partial x} + \frac{\partial q_y}{\partial y} = i_e \tag{5}$$

275   where h is the surface flow depth, q_x and q_y are the unit discharges in the x- and y-directions,

276   respectively, and i_e is the infiltration excess. Manning's equation which considers momentum loss

277   is used to calculate q. In the x-direction:

278
$$q_x = \alpha_x h^\beta \tag{6}$$

279   Where β is a unit dependent coefficient equal to $\frac{5}{3}$, and

280
$$\alpha_x = \frac{S_{fx}^{1/2}}{n_{ov}} \tag{7}$$

281   where n_{ov} is the tunable overland flow roughness coefficient. The momentum equation in the x-

282   direction is given by:

283
$$S_{fx} = S_{ox} - \frac{\partial h}{\partial x} \tag{8}$$

284   where S_{fx} is the friction slope, S_{ox} is the terrain slope, and $\frac{\partial h}{\partial x}$ is the change in surface flow depth

285   in the x-direction.

286   Off-the-shelf, WRF-Hydro does not output overland flow at terrain routing grids (100 m), however

287   it is computed in the background to determine channelized streamflow. One key advance made in

288   this work is that we modified WRF-Hydro source code to output overland flow. Overland flow

289   depth (m) was converted to overland discharge (m^3 s^{-1}) by multiplying flow depth by grid cell area

290   (10,000 m^2) and dividing by the LSM time step (1 h).

291

3.4 Channel routing

If overland flow intersects grid cells identified as channel grids [2nd Strahler stream order and above; pre-defined by the hydrologically conditioned USGS National Elevation Dataset 30-m digital elevation model (DEM)], the channel routing module routes the water as channelized streamflow using a 1-dimensional, explicit, variable time-stepping diffusive wave formulation. Similarly, the continuity equation for channel routing is given as:

$$\frac{\partial A}{\partial t} + \frac{\partial Q}{\partial s} = q_l \tag{9}$$

and the momentum equation is given as:

$$\frac{\partial Q}{\partial t} + \frac{\partial(\frac{\gamma Q^2}{A})}{\partial s} + gA\frac{\partial H}{\partial s} = -gAS_f \tag{10}$$

where s is the streamwise coordinate, H is water surface elevation, A is the flow cross-sectional area calculated as $(B_w + H z)H$ (Fig. B2), q_l is the lateral inflow rate into the channel grid, Q is the flow rate, γ is a momentum correction factor, g is acceleration due to gravity, and S_f is the friction slope computed as:

$$S_f = (\frac{Q}{K})^2 \tag{11}$$

where K is the conveyance computed from the Manning's equation:

$$K = \frac{C_m}{n} AR^{2/3} \tag{12}$$

where n is the Manning's roughness coefficient, A is the channel cross-sectional area, R is the hydraulic radium *(A/P)*, P is the wetted perimeter, and C_m is a dimensional constant (1.486 for English units or 1.0 for SI units).

4 Model simulation, calibration, and validation

4.1 Model domain

The WRF-Hydro model domain spans regions in California including the Coast Ranges, Monterey Bay, and the Central Valley, and covers several burn scars from the 2020 wildfire season (Fig. 1a). Here we focus our analysis on the Dolan burn scar where the hazardous debris flows occurred (Fig. 1b). According to the USGS 30-m DEM, the Rat Creek debris flow site sits at the base of a 1st order catchment with a drainage area of 2.23 km². Mill Creek, Big Creek, and Nacimiento debris flows were initiated within extremely steep, intensely burned, 1st order catchments, but were deposited in 2nd, 3rd, and 3rd Strahler stream order channels, respectively.

To calibrate and validate WRF-Hydro output, we use soil moisture observations from two Physical Sciences Laboratory (PSL) monitoring stations [i.e., Lockwood (lwd) and Gilroy (gry)] (Fig. 1a).

323 Due to the Mediterranean climate of California, many USGS stream gages experience low or no
324 flow during the dry season. In addition, many gages are under manual regulation to mitigate wet-
325 season flood risks and better distribute water resources. As such, it can be challenging to obtain
326 natural streamflow observations for model calibration. Here, three USGS stream gages [i.e.,
327 Arroyo Seco NR Greenfield, CA (ID 11151870), Arroyo Seco NR Soledad, CA (ID 11152000),
328 and Arroyo Seco BL Reliz C NR Soledad, CA (ID 11152050)] (Fig. 1a) on streams that have
329 measurable flows during our study period and are free of human regulation are used. These gages
330 are located downstream of the Dolan burn scar and hence are useful in calibrating the parameters
331 associated with burn scar effects. The PSL soil moisture observations were recorded at 2-minute
332 intervals and USGS streamflow gage data were recorded at 15-minute intervals, but we perform
333 all observation-model comparisons at hourly-mean resolution.

334

335

336 **4.2 Baseline simulation and soil moisture calibration**

337 WRF-Hydro was run from January 1–31 of 2021. We performed the baseline simulation by
338 modifying WRF-Hydro default parameters (Table B3) based on a calibration using soil moisture
339 observations from stations lwd and gry. Neither PSL station is located in a burn scar. Since the
340 baseline simulation includes no postfire characteristics, it can also be regarded as the "pre-fire"
341 scenario. Soil moisture at 10 cm below ground in the baseline simulation was calibrated by
342 performing a domain-wide adjustment of soil porosity and grain size distribution index at the
343 simulation start (Table B3). We then allowed the model to spin up from January 1–10 before using
344 January 11–31 for validation. Using a relatively short spin-up period is justified because prior to
345 the AR event, little rain fell on the Dolan burn scar (i.e., ~400 mm of rainfall fell from June to
346 December 2020). As such, in the months preceding the debris flow events, soil moisture
347 observations indicate already dry condition prior to our 10 day spin up.

348

349 After calibration, the simulated soil moisture closely mimics ground-based PSL observations (Fig.
350 4). Both the observed magnitude and variability are well captured, with the simulated ±1 standard
351 deviation envelope largely encompassing PSL observations during the AR. Model performance
352 was evaluated using four quantitative metrics, i.e., correlation coefficient, root mean square error,
353 mean bias, and Kling-Gupta efficiency (KGE; Gupta et al., 2009; Kling et al., 2012). KGE has
354 previously been used in soil moisture calibration applications (e.g., Lahmers et al., 2019;
355 Vergopolan et al., 2020) and is computed as follows:

356

$$KGE = 1 - \sqrt{(r-1)^2 + (\alpha-1)^2 + (\beta-1)^2} \qquad (13)$$

358

359 where r is the correlation coefficient between the observation and simulation, α is the ratio of the
360 standard deviation of simulation to the standard deviation of observation, and β is ratio of the

361   mean of simulation to the mean of observation. KGEs close to 1 indicate a high-level consistency
362   between the simulation and observation, while negative KGEs indicate poor model performance
363   (Schönfelder et al., 2017; Andersson et al., 2017).
364
365   The model's ability to simulate soil moisture substantially improves after calibration (Fig. 4; Table
366   1). KGE values approach 1 (0.72 at lwd and 0.88 at gry), indicating that WRF-Hydro adequately
367   simulates the hydrologic environment and its response to meteorological change.
368
369
370

MRMS precipitation, observed and simulated soil moisture
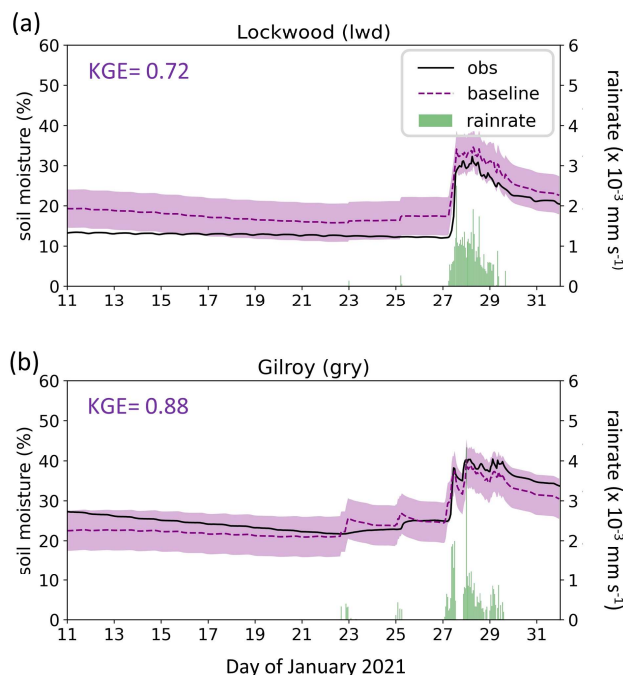
371
372   **Fig. 4|** Precipitation, observed and simulated soil moisture at two PSL soil moisture stations.
373   January 11–31, 2021 MRMS precipitation (green bars) and observed (black line) and simulated
374   volumetric soil moisture 10 cm below ground in the baseline simulation (purple dashed line) at
375   PSL sites (a) Lockwood (lwd) and (b) Gilroy (gry). Envelope of purple shading depicts ±1 standard
376   deviation of model simulated soil moisture. KGE scores are provided at top left for each station.
377
378
379

380 *Table 1*
381 *Evaluation metrics of simulated soil moisture and streamflow*
382

Soil moisture (Default / Baseline)				
Station	*r*	RMSE	Bias	KGE
lwd	0.97 / 0.98	7.06 / 4.32	5.21 / 4.16	0.10 / 0.72
gry	0.94 / 0.94	5.19 / 2.53	-4.79 / -1.66	0.80 / 0.88
Streamflow (Baseline / Burn scar)				
Station	*r*	RMSE	Bias	NSE
1870	0.28 / 0.93	39.29 / 14.69	1.65 / 3.36	-0.17 / 0.84
2000	0.26 / 0.86	51.22 / 24.92	2.47 / 4.81	-0.15 / 0.73
2050	0.25 / 0.81	49.96 / 27.43	5.70 / 8.24	-0.38 / 0.53

383

384 **Table 1|** Quantitative evaluation metrics for the simulated soil moisture and streamflow when
385 compared against observations. The metrics include the Pearson correlation coefficient (*r*), root
386 mean square error (RMSE), and mean bias (Bias). In addition, the comprehensive metrics Kling-
387 Gupta efficiency (KGE) and Nash-Sutcliffe efficiency (NSE) are used to evaluate model-simulated
388 soil moisture and streamflow, respectively. For soil moisture, the numbers in front of "/" are
389 calculated between the default run (i.e., uncalibrated run) and the observations, whereas the
390 numbers following "/" are the corresponding values in the baseline simulation (the purple dashed
391 line in Fig. 4). For streamflow, the numbers in front of "/" are computed between the baseline run
392 (purple dashed line in Fig. 6) and the observations, while the numbers behind "/" are for burn scar
393 simulation (red line in Fig. 6). If the model performance regarding a certain metric is enhanced in
394 the burn scar simulation, the number after "/" is underlined.

395

4.3 Burn scar simulation and streamflow calibration

397 To simulate effects of wildfire burn scars on hydrologic processes and debris flow hazards, we
398 made two modifications to the baseline simulation soil moisture calibrated model configuration.
399 First, we changed the land cover type within the burn scar perimeter to its nearest LSM analogue,
400 i.e., "barren and sparsely vegetated". The switch to barren land causes: (1) height of the canopy
401 (HVT) to decrease to 0.5 m; (2) maximum rate of carboxylation at 25°C (VCMX25) to decrease
402 to 0 $\mu mol\ CO_2/(m^2 \cdot s)$; and (3) overland flow roughness coefficient (OV_ROUGH2D) to decrease
403 to 0.035 (Fig. 5a–c) from default values (Fig. B4 and Table B2).

404

405 The second adjustment was to decrease soil infiltration rates within the burn scar perimeter,
406 achieved by reducing soil saturated hydraulic conductivity (DKSAT; Fig. 5d; Scott & van Wyk,

1990; Cerdà, 1998; Robichaud, 2000; Martin & Moody, 2001) from default values (Table B3). Consistent with the hydrophobicity of burned soils, we calibrate the burn scar simulation by systematically exploring a range of burn scar area saturated hydraulic conductivities (0 to 3×10^{-7} m s^{-1} with a 5×10^{-8} m s^{-1} increment), with the goal of reproducing streamflow behavior similar to USGS gage observations. We found that a value of 1.5×10^{-7} m s^{-1} gives the highest Nash-Sutcliffe efficiency (NSE; Nash & Sutcliffe, 1970) across all three USGS stream gages (Table 1). NSE and KGE are the two most widely used metrics for calibration and evaluation of hydrologic models. The NSE has previously been used in streamflow calibration applications (e.g., Xia et al., 2012; Bitew & Gebremichael, 2011), and it is calculated as follows:

$$NSE = 1 - \frac{\sum_{t=1}^{t=T}(Q_{sim}(t)-Q_{obs}(t))^2}{\sum_{t=1}^{t=T}(Q_{obs}(t)-\overline{Q_{obs}})^2} \qquad (14)$$

where T is the length of the time series, $Q_{sim}(t)$ and $Q_{obs}(t)$ are the simulated and observed discharge at time t, respectively, and $\overline{Q_{obs}}$ is the mean observed discharge. By definition, NSEs of 1 indicate perfect correspondence between the simulated and observed streamflow. Positive NSEs mean that the model streamflow has a greater explanatory power than the mean of the observations, whereas negative NSEs represent poor model performance (e.g., Moriasi et al., 2007; Schaefli & Gupta, 2007). When burn scar characteristics are included, NSEs increase from negative values in the baseline to greater than 0.5, and the NSEs at gages 1870 and 2000 reach 0.84 and 0.73, respectively. Higher NSE scores indicate the abovementioned burn scar parameter changes improve the model's ability to simulate streamflow observations downstream of the burn scar (Table 1).

430
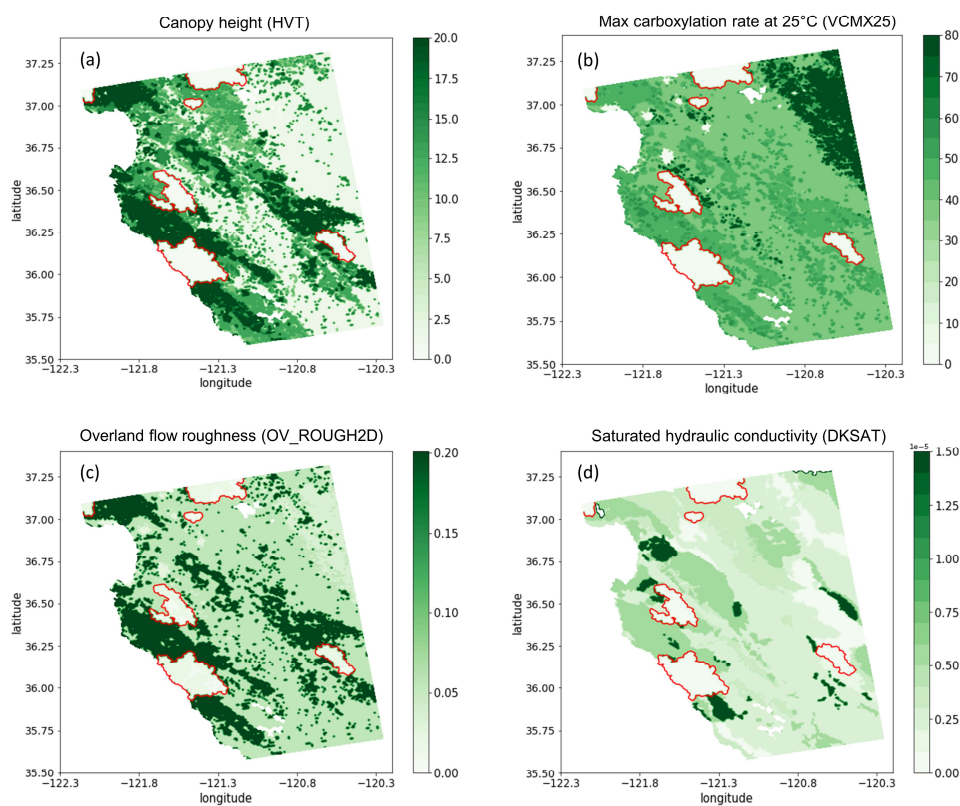
Fig. 5 | Parameter setting in the WRF-Hydro burn scar simulation. (a) The height of the canopy
(HVT; m; shading), (b) maximum rate of carboxylation at 25°C (VCMX25; $\mu mol\ CO_2/(m^2 \cdot s)$;
shading), (c) overland flow roughness coefficient (OV_ROUGH2D; shading), and (d) saturated
hydraulic conductivity (DKSAT; m s^{-1}; shading) in the burn scar simulation.

Fig. 6| Precipitation, observed and simulated streamflow at three USGS stream gages. January 26–31, 2021 MRMS precipitation (green bars), observed (black dash dotted line) and simulated streamflow in baseline simulation (purple dashed line) and burn scar simulation (red line) at (a) Arroyo Seco NR Greenfield, CA (ID 11151870), (b) Arroyo Seco NR Soledad, CA (ID 11152000), and (c) Arroyo Seco BL Reliz C NR Soledad, CA (ID 11152050). NSE scores for baseline (purple) and burn scar simulations (red) are shown at top left.

5 Results

5.1 Hydrologic response due to burn scar incorporation

The pre-fire baseline simulation fails to capture the hydrologic behavior observed at the USGS gages located within the burn scar (Fig. 6). Incorporation of burn scar characteristics substantially alters the hydrologic response of the model and provides much higher fidelity streamflow

449   simulations (Fig. 6). Observed hydrographs are characterized by two early streamflow peaks
450   related to two precipitation bursts on January 27th and 28th. Our burn scar simulation captures this
451   behavior, while the baseline simulation streamflow peaks just once, with a lower magnitude and
452   an ~3-day lag after peak precipitation (Fig. 6). The steep rising limbs and high magnitude discharge
453   peaks of the burn scar hydrograph are indicative of flash flooding. Compared with the pre-fire
454   baseline scenario, the burn scar's barren land and low infiltration rate substantially accelerate
455   drainage rates and increase discharge volume into stream channels.
456

5.2 Hydrologic response at four debris flow sites

458   We identified locations and extent of four debris flows from remote sensing data and field work
459   (Fig. 3& Fig. B1). rdNDVI shows vegetation loss caused by debris flows. Mill Creek, Big Creek,
460   and Nacimiento were relatively large debris flows with runout lengths between ~2–5 km. Rat
461   Creek occurred in a smaller catchment and had a runout length of ~300 m. The difference in runout
462   length and debris flow size is primarily controlled by upstream catchment size. Due to its low
463   stream order (1st Strahler stream order), Rat Creek is the only debris flow site modeled entirely as
464   overland flow in our WRF-Hydro simulations.

465   At the four debris flow sites, we use three metrics to characterize hydrologic anomalies: (1)
466   accumulated runoff volume, (2) peak discharge, and (3) time to peak discharge. Fig. 7 depicts
467   accumulated channelized discharge volume (blue shading) and accumulated overland discharge
468   volume (yellow-red shading) from January 27th 00:00 to 28th 12:00 near the four debris flow sites
469   in the burn scar simulation. Accumulation time period is chosen such that it covers the first two
470   runoff surges in the simulated hydrographs which are likely associated with debris flows (Fig. 8)
471   given that nearly concurrent peak rainfall intensity and peak discharge is a signature characteristic
472   of debris flows (Kean et al., 2011). Runoff volume is on the order of 10^4 m^3 at Rat Creek and 10^6
473   m^3 at the other three sites.

474
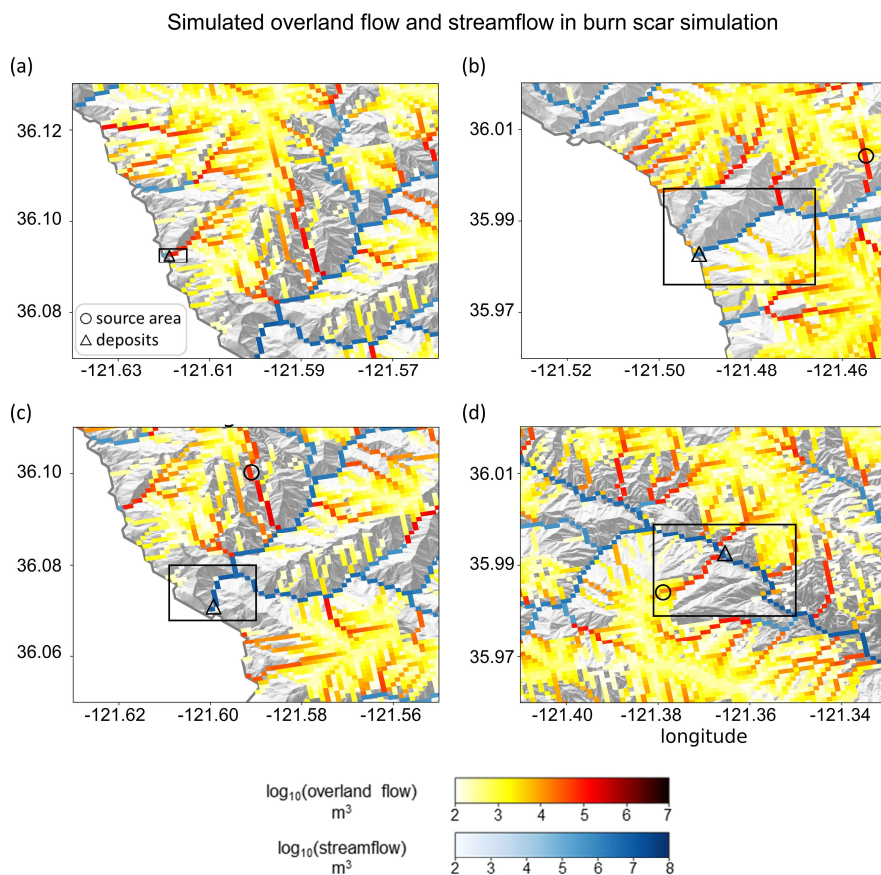
Fig. 7| WRF-Hydro simulated overland flow and streamflow in the burn scar simulation. (a)–(d)
475

Total volume of accumulated overland flow (yellow-red shading) and streamflow (blue shading)
476

on log_{10} scale between January 27th 00:00 and 28th 12:00 at four debris flow sites. Black rectangles
477

correspond to domains in Fig. 3a–d. Black circles and triangles indicate debris flow source areas
478

and deposits, respectively.
479

480

481

Dramatic hydrographic changes after inclusion of burn scar characteristics are simulated at debris
482

flow source areas (Fig. B6 and Table B4) and deposition sites (Fig. 8 and Table 2). WRF-Hydro
483

facilitates investigation of the hydrologic response at triggering and deposition locations and along
484

the runout path. Here, to emphasize the downstream hazards, our analysis is focused on debris
485

flow deposits. At Rat Creek, where a section of CA1 collapsed, the magnitude of discharge
486

substantially increases, and overland flow surges are concurrent with rainfall bursts (Fig. 8a). Total
487

discharge accumulated during the AR event increases approximately eight-fold (791%), and peak
488

489   discharge more than triples compared to the baseline simulation (Fig. 8a and Table 2). At Mill
490   Creek, Big Creek, and Nacimiento, baseline hydrographs are characterized by less variability,
491   muted responses to two early precipitation bursts, and a delayed third discharge peak that does not
492   occur until ~3 days after AR passage (Fig. 8b–d). Maximum discharge peaks in the baseline
493   hydrographs lag those in the burn scar simulation by ~2 days (Fig. 8b–d; Table 2). In the burn scar
494   simulation, total volume substantially increases at the three channelized sites – total volume
495   increases ~650% at Mill Creek, ~891% at Big Creek, and ~829% at Nacimiento (Fig. 8b–d and
496   Table 2), and the absolute increase in volume is on the order of 10^6 m^3 (Table 2). Peak discharge
497   more than triples at Mill Creek and Big Creek and more than quadruples at Nacimiento.
498   Additionally, response times of the peak in discharge to the peak in precipitation decrease to less
499   than an hour, highlighting the simulated flashiness of the burned catchments.

500
501
502
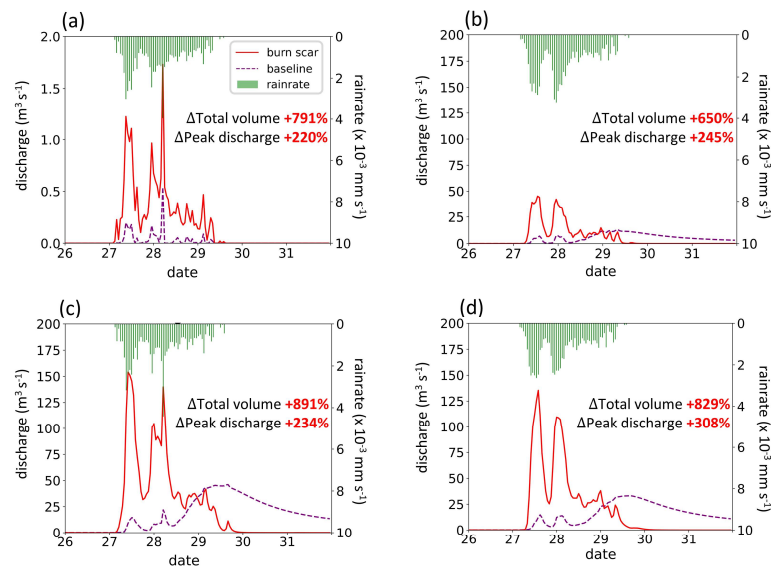
503
504
505   **Fig. 8|** WRF-Hydro simulated discharge time-series at four debris flow deposition locations. (a)–
506   (d) MRMS precipitation (green bars) and simulated discharge time-series for January 26th 00:00
507   to 31st 23:00 at (a) Rat Creek, (b) Mill Creek, (c) Big Creek, and (d) Nacimiento deposition
508   locations (black triangles in Fig. 7a–d) in baseline simulation (purple dashed line) and burn scar
509   simulation (red line).
510
511

512 *Table 2*

513 *The total runoff volume, peak discharge, and peak timing at debris-flow deposits*

Site name	Baseline simulation			Burn scar simulation			
	Total volume (m³)	Peak discharge (m³ s⁻¹)	Highest peak timing	Total volume (m³)	Peak discharge (m³ s⁻¹)	1st Peak timing	2nd Peak timing
Rat Creek	6,897	0.54	28th 05:00	61,425 (+791%)	1.73 (+220%)	27th 09:00	28th 05:00
Mill Creek	312,925	13.10	29th 08:00	2,347,457 (+650%)	45.21 (+245%)	27th 13:00	27th 23:00
Big Creek	842,808	46.10	29th 16:00	8,354,095 (+891%)	154.10 (+234%)	27th 10:00	28th 05:00
Nacimiento	743,531	33.15	29th 16:00	6,904,706 (+829%)	135.41 (+308%)	27th 14:00	28th 00:00

514

515 **Table 2|** The total runoff volume, peak discharge, and peak timing in the baseline and burn scar
516 simulations from January 27th 00:00 to 31st 23:00 at deposition sites of Rat Creek, Mill Creek, Big
517 Creek, and Nacimiento debris flows (black triangles in Fig. 7a–d). The peak timing shown in the
518 baseline simulation is for the highest peak. The percent change of the total volume and peak
519 discharge in the burn scar simulation relative to the baseline simulation are shown in parentheses.

520

521

522 **5.3 Debris flow hazard assessment for the Dolan burn scar**

523 Since high magnitude runoff is often the cause and precursor of runoff-generated debris flows in
524 burned areas (Cannon et al., 2003, 2008; Rengers et al., 2016), we use simulated accumulated
525 volume of overland flow and streamflow to assess runoff-generated debris flow hazard potential
526 under pre-fire (i.e., baseline; Fig. 9a&d) and postfire (i.e., burn scar simulation; Fig. 9b&e)
527 conditions. We assess changes at both stream and catchment levels and use the difference between
528 burn scar and baseline simulations to assess added debris flow hazard potential (Fig. 9c&f).
529 Consistent with the increasing erosive and entrainment power associated with increasing discharge,
530 our debris flow hazard increases as the accumulated discharge volume increases. To reduce the
531 effects of catchment size on the volume-based hazard levels, we normalize a catchment's discharge
532 volume by the area of the catchment (Santi et al., 2012; Fig. 9d–f). Non-normalized catchment
533 hazard maps are also provided (Fig. B7).

534

535 In the pre-fire baseline simulation, the AR-induced precipitation produces lower debris flow
536 hazard over most of the domain, but elevated hazards along stream channels (Fig. 9a). We note no
537 substantial differences between areas in or out of the burn scar. In the burn scar simulation, debris

flow hazard levels increase across the Dolan burn scar and along channels outside but downstream of the burn scar (Fig. 9b–c). The discharge volume increases by an order of magnitude near Rat Creek, Big Creek, Mill Creek, and Nacimiento. Within the burn scar, hazards along major stream channels, such as the Nacimiento River and San Antonio River increase. Outside the burn scar, hazard levels along river channels downstream of the burn scar, such as the Arroyo Seco River, also increase (Fig. 9c).

At the catchment level, debris flow hazards are assessed using accumulated discharge volumes normalized by catchment areas (Fig. 9d–f). Accumulated discharge volumes are assessed at the outlet of each catchment between January 27th 00:00 to 28th 12:00. In the baseline simulation, the majority of catchments are subject to relatively low debris flow hazards compared to the burn scar simulation with total normalized discharge volume less than 10^3 m^3 km^{-2} (Fig. 9d). In the burn scar simulation, over half of catchments within the Dolan burn scar have normalized discharge volume greater than 10^5 m^3 km^{-2}, while over 1/4 of basins reach 10^6 m^3 km^{-2} (Fig. 9e). The additional debris flow hazard brought about by the inclusion of wildfire burn scar characteristics is substantial (Fig. 9f).

To summarize changes in debris flow hazards as a result of including burn scar characteristics in WRF-Hydro simulations, we create distributions of pre-fire baseline and burn scar catchment-area normalized discharge from the 404 catchments located within the Dolan burn scar perimeter (Fig. 10). After incorporating burn scar characteristics, the full distribution shifts to the right, indicating increased hazard levels – a shift considered robust by a Student's t-test (p value: 4.6E-45). A quantitative assessment of this shift indicates that the mean catchment area normalized discharge volume increases by ~1300% (from ~380k to 5.5M m^3 km^{-2}) while the standard deviation increases ~1400% (from ~1.6M to 23.0M m^3 km^{-2}). We also assess shifts at a range of distribution percentiles: 5P: 148% (~0.6k to ~1.5k m^3 km^{-2}), 25P: 725% (~3.7k to ~30.7k m^3 km^{-2}), 50P: 924% (~13k to ~135k m^3 km^{-2}), 75P: 980% (~120k to ~1.3M m^3 km^{-2}), and 95P: 1300% (~2.1M to ~29.1M m^3 km^{-2}). In the burn scar simulation, more than half of catchments have normalized volumes > 10^5 m^3 km^{-2} and more than 1/4 of catchments have volumes > 10^6 m^3 km^{-2} – values that correspond to the 75P and 90P of the baseline simulation, respectively. Disproportionate shifting of the right tail of the distribution suggests that extreme debris flow hazards increase non-linearly under simulated burn scar conditions.

Our catchment-area normalized discharge volume-based hazard assessment also indicates that the catchments containing Mill Creek, Big Creek, and Nacimiento had elevated hazard potential (Fig. 9d–f), consistent with our (limited) debris flow observations. Other areas with elevated hazards include catchments containing the Arroyo Seco and San Antonio Rivers. Beyond the burn scar perimeter, effects of fire expand to adjacent and downstream catchments, and the drainage basins of the Arroyo Seco and Nacimiento Rivers are simulated to have potentially hazardous conditions, i.e., normalized discharge volumes in excess of 10^6 m^3 km^{-2} (Fig. 9e&f).

Stream channel hazard assessment

Normalized catchment hazard assessment
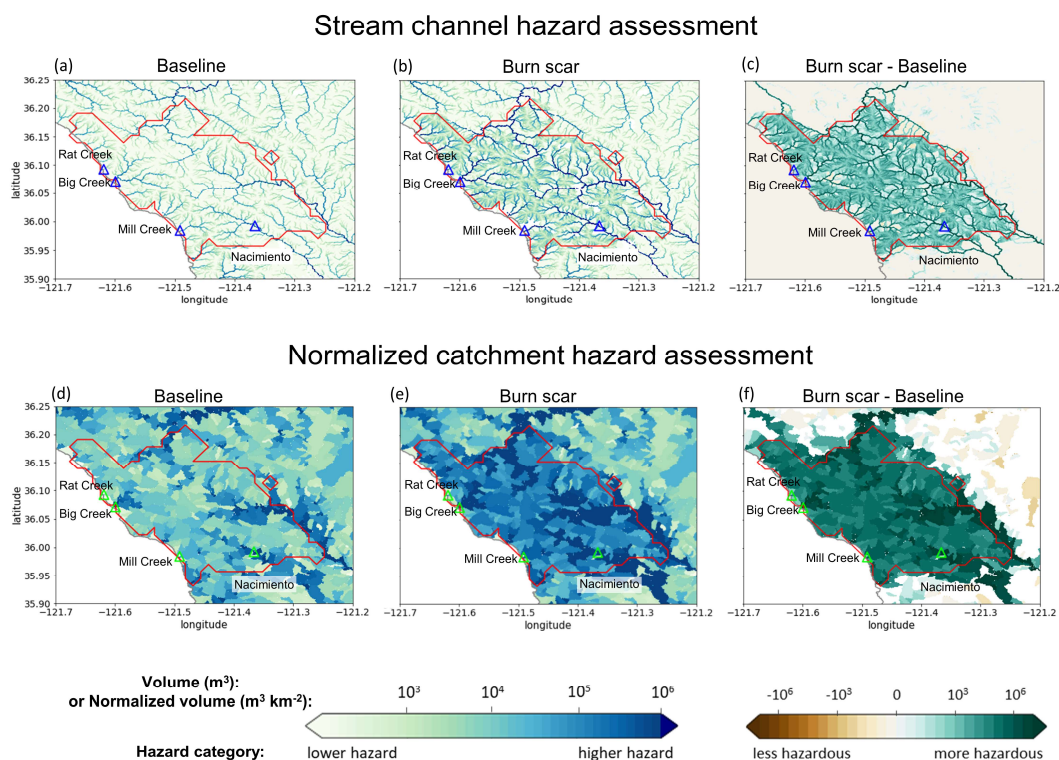
577
578
579 **Fig. 9|** Discharge volume-based runoff-generated debris flow hazards. Debris flow hazards at
580 individual stream level for the (a) baseline, (b) burn scar, and (c) difference between burn scar and
581 baseline simulations. Hazard is estimated as total discharge volume from January 27th 00:00 to
582 28th 12:00. (d)–(f) Normalized debris flow hazards by catchment area at catchment level. For each
583 catchment, the hazard is determined by total discharge volume at the catchment outlet from
584 January 27th 00:00 to 28th 12:00 divided by catchment area.

585
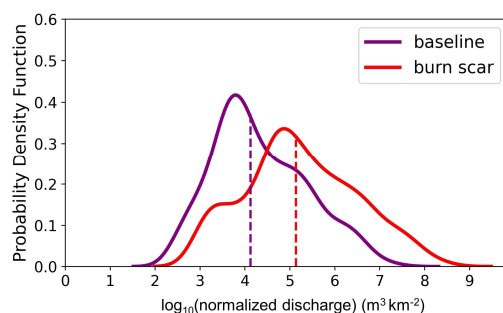
Fig. 10| Distributions of accumulated discharge volumes at the outlet of the 404 catchments
normalized by upstream catchment areas within Dolan burn scar in the baseline simulation (purple
line) and in the burn scar simulation (red line). Dashed vertical lines indicate median values.

5.4 Debris flow hazard assessment at regional scales

While the results we present above primarily focus on hazards in the Dolan burn scar, our WRF-
Hydro domain includes a number of additional 2020 wildfire burn scar sites (Fig. 1a). Given the
long filament-like structure of western U.S. landfalling ARs, the heterogeneous nature of
landfalling trajectories, and the potential for systems to interact with diverse topographic terrains,
the development of tools capable of regional hazard assessments under high-gradient precipitation
events is crucial – particularly in a wildfire-prone region like California. To demonstrate the
potential utility of WRF-Hydro in regional applications, we assess hazards over our full domain
(Fig. 11). We find that hazard potential, from both channelized and overland flows, is greatest
within the burn scar sites, with maximum hazards found in the Dolan burn scar, consistent with
the location of elevated precipitation along the Coast Ranges – where more than 300 mm of rain
fell over three days (Fig. 11). Other high hazard-elevated precipitation regions within our domain
include the western edge of the Sierra Nevada and areas north of Monterey Bay, which collocate
with the Mineral and Del Puerto burn scars, respectively. Similar to our Dolan burn scar focused
analysis, areas within and downstream of these burn scar sites have elevated streamflow discharge
volumes compared to the non-burned areas (Fig. 11b). Likewise, areas of heightened accumulated

605   overland flow are elevated in burn scar regions, but also demonstrate a strong correspondence to

606   the spatial distribution of precipitation (Fig. 11a & c).
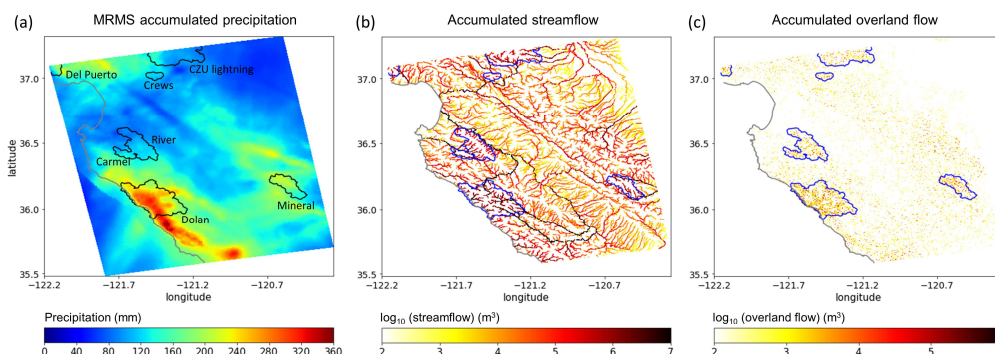
607

608   **Fig. 11|** MRMS accumulated precipitation and regional debris flow hazard assessment. (a) MRMS

609   accumulated precipitation during January 27th 00:00 to 29th 23:00 over the model domain

610   (shading; mm). Names of burn scars are labeled in black. (b) Accumulated streamflow (yellow-to-

611   red shading; m^3) and (c) accumulated overland flow from 27th 00:00 to 28th 12:00 over the model

612   domain (yellow-to-red shading; m^3). Wildfire perimeters of 2020 wildfire season are outlined in

613   black in (a), and in blue in (b) and (c). The coastline of California is in grey.

614

6 Discussion

616   Given the historic and growing frequency of wildfires in the western U.S. (Swain 2021; Williams

617   et al., 2019; Goss et al., 2020) and globally (Jolly et al., 2015; Flannigan et al., 2013), developing

618   tools to investigate, better understand, and potentially predict changes in burn scar hydrology and

619   natural hazards at regional scales is critical. Here, we demonstrate the first use of WRF-Hydro to

620   simulate the surface hydrologic response over a burn scar during a landfalling AR. We augmented

621   the default version of WRF-Hydro to output overland flow and to replicate burn scar behavior by

622   adjusting vegetation type and infiltration rate parameters. WRF-Hydro simulations were validated

623   against PSL soil moisture and USGS streamflow observations before we used simulated

624   streamflow and overland flow volumes to characterize debris flow hazard potential.

625

626   A comparison between baseline and burn scar simulations demonstrated that changes in hydraulic

627   properties of burned areas causes drastic changes in surface flows, including faster discharge

628   response times, greater discharge volumes, and overall flashier hydrologic behavior in surface

629   flows. As a result of including bur scar characteristics in WRF-Hydro simulations, median

630   catchment-area normalized discharge volume increases nine-fold, while 95P volume increases 13-

631   fold. The magnitude of our simulated changes is consistent with findings from previous postfire
632   hydrology studies (Anderson et al., 1976; Scott, 1993; Meixner & Wohlgemuth, 2003; Kinoshita
633   & Hogue, 2015; Kean et al., 2011). At Rat Creek, where a debris flow destroyed CA1, our model
634   simulation predicted an eight-fold increase in accumulated overland flow and a tripling in peak
635   discharge when compared to the baseline simulation. At Mill Creek, Big Creek, and Nacimiento,
636   the increase of runoff volume from the baseline to the burn scar simulation is on the order of 10^6
637   m³. Our hazard assessments based on catchment-area normalized discharge volumes indicated that
638   Mill Creek, Big Creek, and Nacimiento were under elevated debris flow hazards, corresponding
639   well with identified debris flow occurrences.
640
641   Despite methodological differences, our debris flow hazard assessment for this AR event is
642   generally consistent with the USGS' postfire, pre-AR, design-storm-based preliminary hazard
643   assessment (USGS, 2020). As described above, USGS preliminary hazard assessments use logistic
644   regression models to estimate the likelihood of debris flow occurrence and multivariate linear
645   regression models to estimate debris flow volumes. This empirical approach is trained on historical
646   western U.S. debris flow occurrence and magnitude data and incorporates estimated burn scar soil
647   erodibility and burn severity data (Cannon et al., 2010; Gartner et al., 2014; Staley et al., 2016).
648   For precipitation, the USGS assessment utilizes a design storm approach that assumes 1–5 year
649   return interval magnitude precipitation falls uniformly over a region/burn scar (USGS, 2020). For
650   the Dolan burn scar, both assessments find that large stream channels had relatively higher hazard
651   levels than small streams or overland areas. However, close comparison of hazard maps reveals
652   differences in spatial distribution of high-hazard catchments. In the USGS assessment, higher
653   hazard levels are predicted north and southeast of the burn scar, whereas in our assessment the
654   highest hazards occur along major stream channels. We hypothesize that USGS-assessed areas of
655   higher hazard potential are related to their use of design-storm precipitation (see Fig. 2 for MRMS
656   precipitation footprint) and burn severity data (Burned Area Emergency Response, 2020).
657   Comparison with the USGS assessment framework suggests room for improvement in WRF-
658   Hydro-based assessments (i.e., inclusion of burn severity and soil erodibility data), but also
659   highlights the potential utility of working with spatially-distributed and time-varying precipitation.
660   However, this also means the accuracy of WRF-Hydro predictions depends on the accuracy of
661   precipitation forcing, and in our hindcast application, MRMS precipitation data (Appendix A).
662   Accordingly, our WRF-Hydro-based hazard assessment could benefit from precipitation products
663   mosaiced from various sources to constrain precipitation-based uncertainties (e.g., gauge-
664   corrected and/or Mountain Mapper MRMS), although the long processing time of these datasets
665   inhibits timely post-event assessments.
666
667   As a water-only model, WRF-Hydro is currently restricted to simulating the hydrologic ingredients
668   of debris flows. While water-only models have been widely used to investigate and better
669   understand debris flow dynamics (Arattano & Savage, 1994; Arattano & Franzi, 2010; Rengers et
670   al., 2016; McGuire & Youberg, 2020; Di Cristo et al., 2021), sediment supply, soil erodibility, and

671 other sedimentological factors also play important roles in determining the potential for and
672 severity of mass failure events (McGuire et al., 2017). Developing a debris flow model that couples
673 hydrologic and sediment erosion and transport processes would represent a significant advance
674 and be of great practical use (Banihabib et al., 2020; Shen et al., 2021). At a minimum, soil grain
675 size maps and domain-specific rainfall intensity-duration curves can provide guidance to define
676 transitions from water floods to debris flows if historical debris flow data is available in the study
677 domain (McGuire & Youberg, 2020; Tognacca et al., 2000; Gregoretti & Fontana, 2008; Cannon
678 et al., 2007).

679

680 **7 Conclusion**

681

682 Use of WRF-Hydro to simulate runoff-generated debris flow hazards in burn scar settings
683 represents a novel application. It is notable that in this application we have balanced the
684 computational cost of a regional domain with our choice of resolved spatial resolution for terrain
685 routing and overland flow calculations (100 m). However, WRF-Hydro has previously been
686 applied to smaller domains at higher terrain routing resolutions (~30 m). Future work could assess
687 the use of the model to study burn scar hydrology at finer spatial scales, should the application
688 warrant and should underlying data at sufficient resolution exist. Other potential applications of
689 our modified model framework include alpine areas and steep hillslopes with sparse vegetation
690 where runoff-generated debris flows dominate over landslide-initiated ones (Davies et al., 1992;
691 Coe et al., 2003, 2008).

692

693 Further, our burn scar parameter changes are performed to Noah-MP, which is the core land
694 surface component of the National Centers for Environmental Prediction Global Forecast System
695 (GFS) and Climate Forecast System (CFS), thus the findings presented herein, are likely to prove
696 useful in the broader worlds of forecast meteorology and climate science. In addition, here WRF-
697 Hydro is driven by historical precipitation and meteorological data, i.e., in hindcast mode. We see
698 no reason why this modeling framework could not also be employed to project hazards under
699 future climatic conditions (e.g., Huang et al., 2020), or given its relatively low computational
700 expense, in operational forecast mode. Indeed, modern ensemble-based meteorological forecasting
701 could provide high spatiotemporal forcing data with which disaster preparedness managers could
702 probabilistically assess debris flow hazard potential, and issue advanced life and property saving
703 warnings.

704
705
706

Appendix A

Text A1. Multi-Radar/Multi-Sensor System (MRMS) radar-only precipitation estimate and uncertainty

MRMS is a precipitation product that covers the contiguous United States (CONUS) on 1-km grids. It combines precipitation estimates from sensors and observational networks (Zhang et al., 2011, 2014, 2016), and is produced at the National Centers for Environmental Prediction (NCEP) and distributed to National Weather Service forecast offices and other agencies. Input datasets used to produce MRMS include the U.S. Weather Surveillance Radar-1988 Doppler (WSR-88D) network and Canadian radar network, Parameter-elevation Regressions on Independent Slopes Model (PRISM; Daly et al. 1994, 2017), Hydrometeorological Automated Data System (HADS) gauge data with quality control (Qi et al., 2016), and outputs from numerical weather prediction models. There are four different MRMS quantitative precipitation estimates (QPE) products incorporating different input data or combinations: radar only, gauge only, gauge-adjusted radar, and Mountain Mapper. For our study period (i.e., January 1–31, 2021), only the radar-only QPE is currently available.

We acknowledge that precipitation data has uncertainties. Use of different precipitation products may produce different results. A study comparing different gridded precipitation datasets including satellite-based precipitation data, gauge dataset, and multi-sensor products revealed large uncertainties in precipitation intensity (Bytheway et al., 2020). However, comparing different precipitation datasets to characterize uncertainties is beyond the scope of this study. MRMS provides gridded precipitation at high temporal (hourly) and spatial (1-km) resolutions, making it a useful tool to demonstrate the utility of WRF-Hydro in post-wildfire debris flow hazard assessments.

731   **Appendix B**
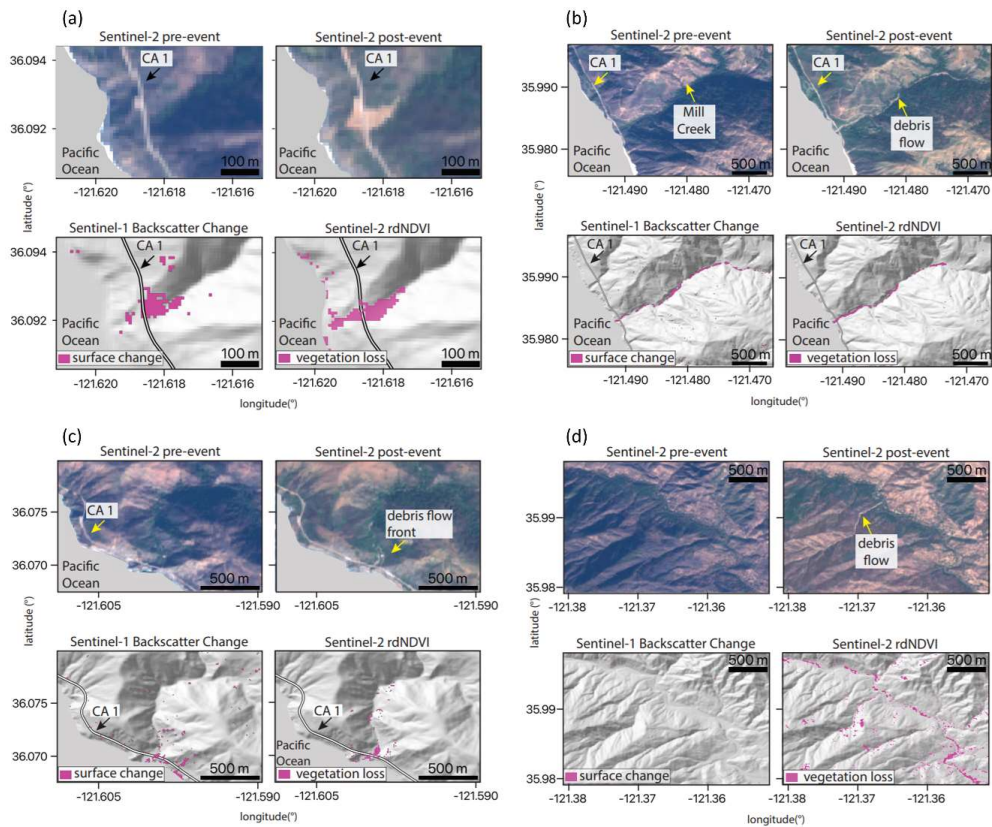
732
733
734   **Fig. B1** Optical- and SAR-based remote sensing data of four debris flows. Optical data from
735   Sentinel-2 show pre- and post-debris flow imagery in real color. rdNDVI calculated from the
736   Sentinel-2 data show a decrease in vegetation corresponding to debris flow locations. Sentinel-1
737   backscatter change shows the change in ground surface properties determined by calculating the
738   log ratio of pre- and post-event SAR images. The pre-event, post-event satellite images, Sentinel-
739   1 Backscatter, and Sentinel-2 rdNDVI change at (a) Rat Creek, (b) Mill Creek, (c) Big Creek, and
740   (d) Nacimiento.
741
742
743

744
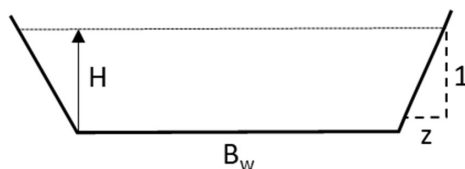
Fig. B2 Schematic trapezoidal shape and related parameters of channels in WRF-Hydro. B_w is the channel bottom width (m), z is the channel side slope (m), and H is water elevation (m). The cross-sectional area of flow is calculated as $(B_w + H z)H$.

748

749   **Table B1 Parameters of trapezoidal channels in WRF-Hydro.**

Stream order	Channel bottom width B_w (m)	Channel side slope z (m)	Manning's roughness coefficient n
1	1.5	3	0.33
2	3	1	0.21
3	5	0.5	0.09
4	10	0.18	0.06
5	20	0.05	0.04
6	40	0.05	0.03
7	60	0.05	0.02
8	70	0.05	0.02
9	80	0.05	0.01
10	100	0.05	0.01

750

751   **Table B1** Parameters of the trapezoidal channels in WRF-Hydro including channel bottom width

752   B_w (m), channel side slope z (m), and Manning's roughness coefficient n.

753

754
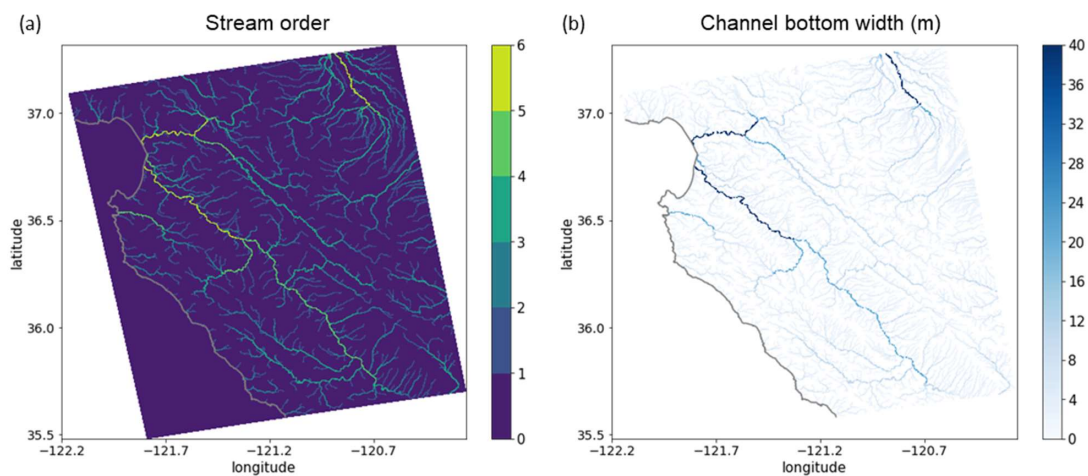
Fig. B3 (a) Stream order defined by the USGS 30-m DEM in our WRF-Hydro model domain
and (b) the channel bottom width (m) which is a function of stream order (Table B1).

759 *Table B2*

760 *MODIS IGBP 20-category land cover type and properties in Noah-MP LSM*

Land cover code	Land cover type	Canopy height (m)	Max carboxylation rate at 25°C ($\mu mol\ CO_2/(m^2 \cdot s)$)	Overland flow roughness
1	Evergreen Needleleaf Forest	20	50	0.2
2	Evergreen Broadleaf Forest	20	60	0.2
3	Deciduous Needleleaf Forest	18	60	0.2
4	Deciduous Broadleaf Forest	16	60	0.2
5	Mixed Forests	16	55	0.2
6	Closed Shrublands	1.1	40	0.055
7	Open Shrublands	1.1	40	0.055
8	Woody Savannas	13	40	0.055
9	Savannas	10	40	0.055
10	Grasslands	1	40	0.055
11	Permanent wetlands	5	50	0.07
12	Croplands	2	80	0.035
13	Urban and Built-Up	15	0	0.025
14	Cropland/natural vegetation mosaic	1.5	60	0.035
15	Snow and Ice	0	0	0.01
16	Barren or Sparsely Vegetated	0	0	0.035
17	Water	0	0	0.005
18	Wooded Tundra	4	50	0.055
19	Mixed Tundra	2	50	0.055
20	Barren Tundra	0.5	50	0.055

761

762 **Table B2** MODIS IGBP 20-category land cover type and properties in Noah-MP LSM.

763

764
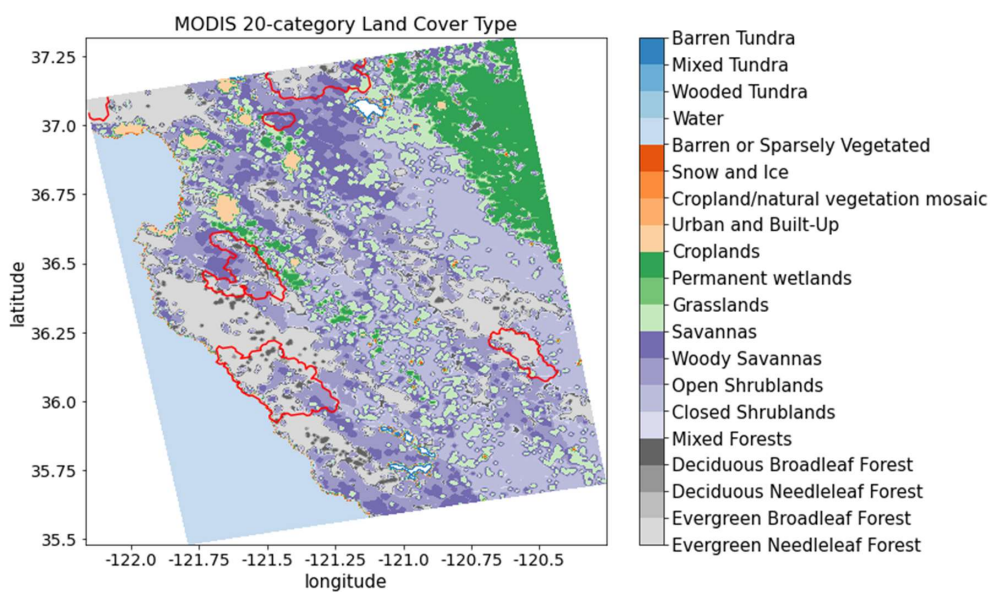
765 **Fig. B4** MODIS IGBP 20-category land cover type in the model domain. Red polylines are 2020

766 wildfire burn scar perimeters.

767

768
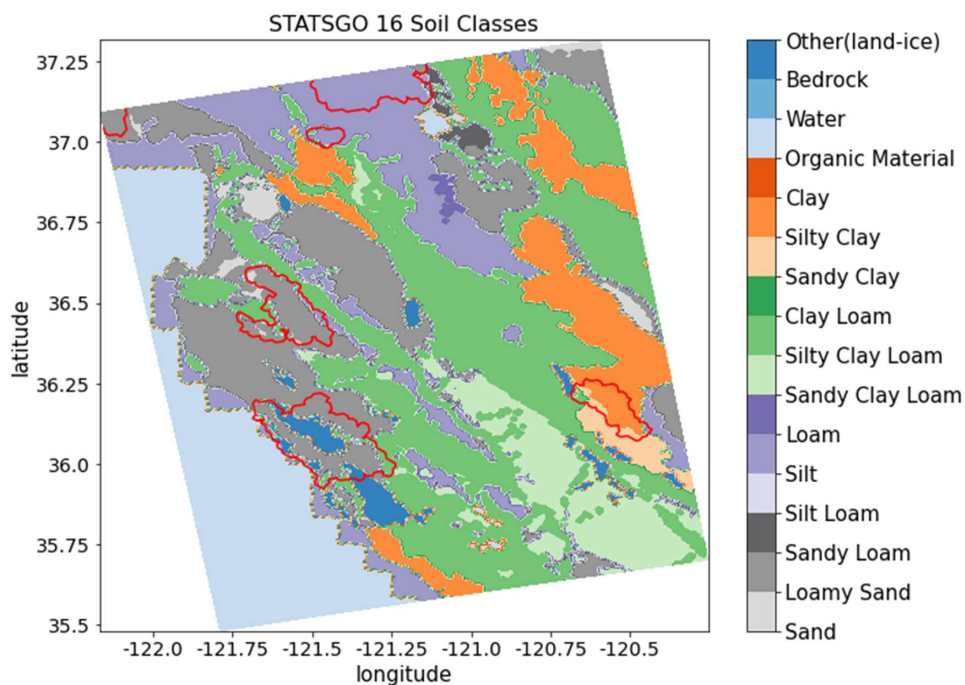
769 **Fig. B5** 1-km STATSGO data with 16 soil texture types. Red polylines are 2020 wildfire burn
770 scar perimeters.

771
772
773
774
775

Table B3

Default and calibrated soil parameters in WRF-Hydro

Soil type	Default			After calibration		
	Grain size distribution index	Porosity	Saturated hydraulic conductivity (m s^{-1})	Grain size distribution index	Porosity	Saturated hydraulic conductivity (m s^{-1})
Sand	2.79	0.339	4.66E-5	2.51	0.315	
Loamy sand	4.26	0.421	1.41E-5	3.83	0.392	
Sandy loam	4.74	0.434	5.23E-6	4.27	0.404	
Silt loam	5.33	0.476	2.81E-6	4.80	0.442	
Silt	3.86	0.484	2.18E-6	3.47	0.450	
Loam	5.25	0.439	3.38E-6	4.73	0.408	
Sandy clay loam	6.77	0.404	4.45E-6	6.09	0.376	
Silty clay loam	8.72	0.464	2.03E-6	7.85	0.432	1.5×10^{-7} m s^{-1} for all the burn scars, and original values elsewhere.
Clay loam	8.17	0.465	2.45E-6	7.35	0.432	
Sandy clay	10.73	0.406	7.22E-6	9.66	0.378	
Silty clay	10.39	0.468	1.34E-6	9.35	0.435	
Clay	11.55	0.468	9.74E-7	10.40	0.435	
Organic material	5.25	0.439	3.38E-6	4.73	0.408	
Water	0.00	1.00	0.00	0.00	1.00	
Bedrock	2.79	0.200	1.41E-4	2.51	0.186	
Other	4.26	0.421	1.41E-5	3.83	0.392	
Playa	11.55	0.468	9.74E-7	10.40	0.435	
Lava	2.79	0.200	1.41E-4	2.51	0.186	
White sand	2.79	0.339	4.66E-5	2.51	0.315	

Table B3 Soil parameters in default and calibrated WRF-Hydro. Default soil parameters in WRF-Hydro are adapted from the soil analysis by Cosby et al. (1984). Grain size distribution index and soil porosity are altered from default values during the global soil moisture calibration. Saturated hydraulic conductivity is altered from default values during the streamflow calibration.
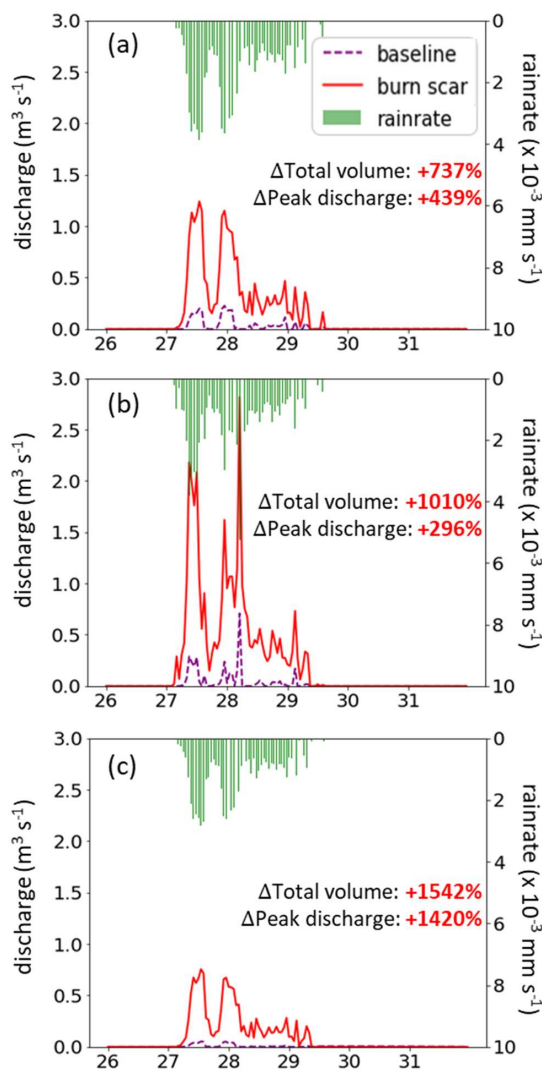
786
787
788 **Fig. B6** WRF-Hydro simulated discharge time-series at four debris flow source areas. (a)–(c)
789 MRMS precipitation (green bars) and simulated discharge time-series for January 26th 00:00 to
790 31st 23:00 at Mill Creek, Big Creek, and Nacimiento debris flow source areas (black circles in Fig.
791 7b–d) in baseline (purple dashed line) and burn scar simulation (red line).
792
793
794
795
796
797

Table B4

The total runoff volume, peak discharge, and peak timing at debris-flow source areas

Site name	Baseline simulation			Burn scar simulation		
	Total volume (m³)	Peak discharge (m³ s⁻¹)	Peak timing	Total volume (m³)	Peak discharge (m³ s⁻¹)	Peak timing
Mill Creek	10,023	0.23	27th 23:00	83,853 (+737%)	1.24 (+439%)	27th 13:00
Big Creek	11,611	0.71	28th 05:00	128,879 (+1010%)	2.81 (+296%)	28th 05:00
Nacimiento	3,031	0.05	27th 13:00	49,792 (+1542%)	0.76 (+1420%)	27th 13:00

Table B4 The total runoff volume, peak discharge, and peak timing in the baseline and burn scar simulations from January 27th 00:00 to 31st 23:00 at source areas of Rat Creek, Mill Creek, Big Creek, and Nacimiento debris flows (black circles in Fig. 7b–d). The percent change of the total volume and peak discharge in the burn scar simulation relative to the baseline simulation are shown in parentheses.

808

809
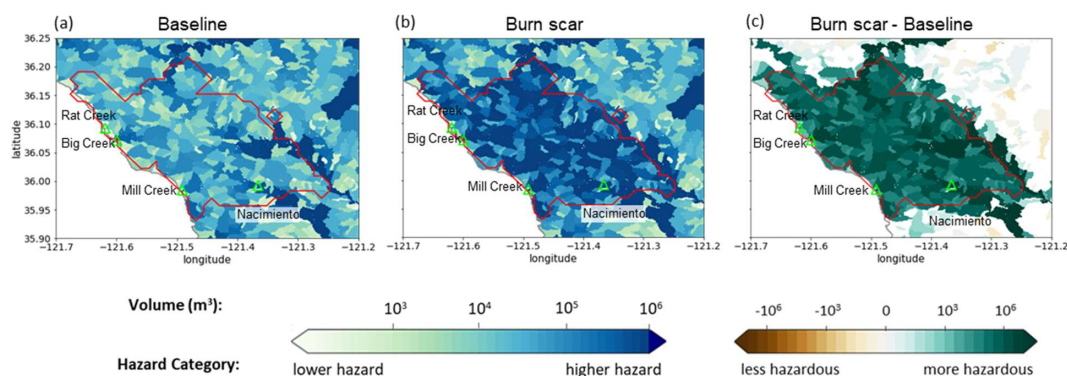
Fig. B7 Discharge volume-based runoff-generated debris flow hazard at catchment level in the (a)
baseline simulation, (b) burn scar simulation, and (c) the difference between the burn scar and
baseline simulations. For each catchment, the hazard is assessed by computing the total discharge
volume at the catchment outlet from January 27th 00:00 to 28th 12:00.

814

815

Data availability statement

The NLDAS-2 reanalysis forcing data is publicly available at NASA GES DISC:
https://disc.gsfc.nasa.gov/datasets?keywords=NLDAS. A detailed description can be found at
https://ldas.gsfc.nasa.gov/nldas/v2/forcing. The MRMS radar-only precipitation estimate is
publicly available at: https://mtarchive.geol.iastate.edu/. A description can be found at
https://www.nssl.noaa.gov/projects/mrms/. The PSL in-situ soil moisture data is publicly available
at: https://psl.noaa.gov/data/obs/datadisplay/. The USGS streamflow is publicly available at:
https://waterdata.usgs.gov/nwis/. The remote sensing data used in this manuscript were provided
by the European Space Agency (ESA) Copernicus program and accessed on Google Earth Engine
(https://code.earthengine.google.com). All processed data required to reproduce the results of this
study are archived on Zenodo at http://doi.org/10.5281/zenodo.5544083.

Code availability statement

The modified WRF-Hydro Fortran code and instructions to output the overland flow at terrain routing grid can be downloaded at https://github.com/NU-CCRG/Modified-WRF-Hydro.

HazMapper v1.0 is available at https://hazmapper.org/. The SAR backscatter change method code is available at https://github.com/MongHanHuang/GEE_SAR_landslide_detection.

Author contribution

Conceptualization: CL, ALH, & DEH; Simulation and model analysis: CL; JW & WY model methodological development. Remote sensing analysis: ALH; Field Observations: NJF; GIS assistance: YX; Funding acquisition: GB & DH; CL wrote the original draft and all authors reviewed and edited the manuscript.

Competing interests

The authors declare that they have no conflict of interest.

Acknowledgments

C.L., A.L.H., J.W., X.L., G.B., and D.E.H. acknowledge support from NSF PREEVENTS #1848683. We acknowledge high-performance computing support from Cheyenne (doi:10.5065/D6RX99HX) provided by NCAR's Computational and Information Systems Laboratory, sponsored by the National Science Foundation.

References

Anderson, H. W., Hoover, M. D., & Reinhart, K. G. (1976). Forests and water: effects of forest management on floods, sedimentation, and water supply (Vol. 18): Department of Agriculture, Forest Service, Pacific Southwest Forest and Range Experiment Station, Berkeley, CA.

Andersson, J. C. M., Arheimer, B., Traoré, F., Gustafsson, D., & Ali, A. (2017). Process refinements improve a hydrological model concept applied to the Niger River basin. Hydrological Processes, 31(25), 4540-4554. doi:https://doi.org/10.1002/hyp.11376

Arattano, M., & Franzi, L. (2010). On the application of kinematic models to simulate the diffusive processes of debris flows. Nat. Hazards Earth Syst. Sci., 10(8), 1689-1695. doi:10.5194/nhess-10-1689-2010

Arattano, M., & Savage, W. Z. J. B. o. t. I. A. o. E. G.-B. d. l. A. I. d. G. d. l. I. (1994). Modelling debris flows as kinematic waves. 49, 3-13.

Banihabib, M. E., Jurik, L., Kazemi, M. S., Soltani, J., & Tanhapour, M. (2020). A Hybrid Intelligence Model for the Prediction of the Peak Flow of Debris Floods. Water, 12(8). doi:10.3390/w12082246

859 Bart, R. (2016). A regional estimate of postfire streamflow change in California. Water Resources Research, 52,
860   n/a-n/a. doi:10.1002/2014WR016553
861 Bart, R., & Hope, A. (2010). Streamflow response to fire in large catchments of a Mediterranean-climate region
862   using paired-catchment experiments. Journal of Hydrology, 388, 370-378.
863   doi:10.1016/j.jhydrol.2010.05.016
864 Bisson M, Favalli M, Fornaciai A, Mazzarini F, Isola I, Zanchetta G, Pareschi MT (2005) A rapid method to
865   assess fire-related debris flow hazard in the Mediterranean region: An example from Sicily (southern
866   Italy) International Journal of Applied Earth Observation and Geoinformation 7:217-231
867   doi:https://doi.org/10.1016/j.jag.2005.04.003
868 Bitew, M. M., & Gebremichael, M. (2011). Assessment of satellite rainfall products for streamflow simulation
869   in medium watersheds of the Ethiopian highlands. Hydrol. Earth Syst. Sci., 15(4), 1147-1155.
870   doi:10.5194/hess-15-1147-2011
871 Brown, E.K., Wang, J., & Feng, Y. (2020). U.S. wildfire potential: a historical view and future projection using
872   high-resolution climate data. Environmental Research Letters. 16, 034060
873 Bytheway, J. L., Hughes, M., Mahoney, K., & Cifelli, R. (2020). On the Uncertainty of High-Resolution Hourly
874   Quantitative Precipitation Estimates in California, Journal of Hydrometeorology, 21(5), 865-879.
875   Retrieved Oct 25, 2021, from https://journals.ametsoc.org/view/journals/hydr/21/5/jhm-d-19-
876   0160.1.xml
877 Camera, C., Bruggeman, A., Zittis, G., Sofokleous, I., & Arnault, J. (2020). Simulation of extreme rainfall and
878   streamflow events in small Mediterranean watersheds with a one-way-coupled atmospheric-hydrologic
879   modelling system. Natural hazards and earth system sciences, 20(10), 2791-2810. doi:10.5194/nhess-
880   20-2791-2020
881 Canfield, H., Goodrich, D., & Burns, I. S. (2005). Selection of Parameters Values to Model Postfire Runoff and
882   Sediment Transport at the Watershed Scale in Southwestern Forests.
883 Cannon, S., Gartner, J, C, P., & Parise, M. (2003). Widlfire-related debris flow generation through episodic
884   progressive sediment-bulking processes, western USA (Vol. 1).
885 Cannon, S., Gartner, J., Wilson, R., Bowers, J., & Laber, J. (2008). Storm Rainfall Conditions for Floods and
886   Debris Flows from Recently Burned Basins in Southwestern Colorado and Southern California.
887   Geomorphology, 96, 250-269. doi:10.1016/j.geomorph.2007.03.019
888 Cannon, S. H. (2001). Debris flow generation from recently burned watersheds. Environmental & Engineering
889   Geoscience, 7(4), 321-341.
890 Cannon, S. H., Boldt, E. M., Laber, J. L., Kean, J. W., & Staley, D. M. J. N. H. (2011). Rainfall intensity–
891   duration thresholds for postfire debris flow emergency-response planning. 59(1), 209-236.
892 Cannon, S. H., & DeGraff, J. (2009). The increasing wildfire and postfire debris flow threat in western USA,
893   and implications for consequences of climate change. In Landslides–disaster risk reduction (pp. 177-
894   190): Springer.
895 Cannon, S. H., Gartner, J. E., Rupert, M. G., Michael, J. A., Rea, A. H., & Parrett, C. (2010). Predicting the
896   probability and volume of postwildfire debris flows in the intermountain western United States. GSA
897   Bulletin, 122(1-2), 127-144. doi:10.1130/B26459.1
898 Cerdà, A. (1998). Changes in overland flow and infiltration after a rangeland fire in a Mediterranean scrubland.
899   Hydrological Processes, 12(7), 1031-1042. doi:https://doi.org/10.1002/(SICI)1099-
900   1085(19980615)12:7<1031::AID-HYP636>3.0.CO;2-V
901 Chen, F., & Dudhia, J. (2001). Coupling an Advanced Land Surface–Hydrology Model with the Penn State–
902   NCAR MM5 Modeling System. Part I: Model Implementation and Sensitivity, Monthly Weather
903   Review, 129(4), 569-585. Retrieved Oct 24, 2021, from

904   https://journals.ametsoc.org/view/journals/mwre/129/4/1520-
905   0493_2001_129_0569_caalsh_2.0.co_2.xml

906 Chen, L., Berli, M., & Chief, K. (2013). Examining Modeling Approaches for the Rainfall-Runoff Process in
907   Wildfire-Affected Watersheds: Using San Dimas Experimental Forest. JAWRA Journal of the
908   American Water Resources Association, 49(4), 851-866. doi:https://doi.org/10.1111/jawr.12043

909 Reynolds, C., (2021, February 25). Highway 1 washout near Big Sur expected to be fixed by summer, Los
910   Angeles Times. https://www.latimes.com/travel/story/2021-02-25/highway-1-to-big-sur-will-reopen-
911   by-summer-caltrans-says

912 Coe, J., Godt, J., Parise, M., & Moscariello, A. (2003). Estimating debris flow probability using fan stratigraphy,
913   historic records, and drainage-basin morphology, Interstate 70 highway corridor, central Colorado, USA.
914   Paper presented at the Debris flow Hazards Mitigation: Mechanics, Prediction, and Assessment, edited
915   by: Rickenmann, D. and Cheng, Ch., Proceedings 3rd International DFHM Conference, Davos,
916   Switzerland.

917 Coe, J. A., Kinner, D. A., & Godt, J. W. J. G. (2008). Initiation conditions for debris flows generated by runoff
918   at Chalk Cliffs, central Colorado. 96(3-4), 270-297.

919 Cosby, B. J., Hornberger, G. M., Clapp, R. B., & Ginn, T. R. (1984). A Statistical Exploration of the
920   Relationships of Soil Moisture Characteristics to the Physical Properties of Soils. Water Resources
921   Research, 20(6), 682-690. doi:https://doi.org/10.1029/WR020i006p00682

922 Cydzik, K., & Hogue, T. S. J. J. J. o. t. A. W. R. A. (2009). Modeling postfire response and recovery using the
923   hydrologic engineering center hydrologic modeling system (HEC-HMS) 1. 45(3), 702-714.

924 Daly, C., R. P. Neilson, & D. L. Phillips. (1994). A statistical-topographic model for mapping climatological
925   precipitation over mountainous terrain. J. Appl. Meteor., 33, 140–158, https://doi.org/10.1175/1520-
926   0450(1994)033<0140:ASTMFM>2.0.CO;2.

927 Daly, C., M. E. Slater, J. A. Roberti, S. H. Laseter, & L. W. Swift Jr.. (2017). High-resolution precipitation
928   mapping in a mountainous watershed; Ground truth for evaluating uncertainty in a national precipitation
929   dataset. Int. J. Climatol., 37, 124–137, https://doi.org/10.1002/joc.4986.

930 Davies, T., Phillips, C., Pearce, A., & Zhang, X. J. I. P. (1992). Debris flow behaviour–an integrated overview.
931   209(21), 225.

932 Dekker, L. W., & Ritsema, C. J. (1994). How water moves in a water repellent sandy soil: 1. Potential and actual
933   water   repellency.   Water   Resources   Research,   30(9),   2507-2517.
934   doi:https://doi.org/10.1029/94WR00749

935 Di Cristo, C., Iervolino, M., Moramarco, T., & Vacca, A. (2021). Applicability of Diffusive model for mud-
936   flows: An   unsteady   analysis.   Journal   of   Hydrology,   600,   126512.
937   doi:https://doi.org/10.1016/j.jhydrol.2021.126512

938 Doerr, S. H., & Thomas, A. (2000). The role of soil moisture in controlling water repellency: New evidence
939   from forest soils in Portugal. Journal of Hydrology, 231-232, 134-147. doi:10.1016/S0022-
940   1694(00)00190-6

941 Friedel, M.J. (2011a) A data-driven approach for modeling post-fire debris-flow volumes and their uncertainty
942   Environmental Modelling & Software 26:1583-1598 doi:https://doi.org/10.1016/j.envsoft.2011.07.014

943 Friedel, M.J. (2011b) Modeling hydrologic and geomorphic hazards across post-fire landscapes using a self-
944   organizing   map   approach   Environmental   Modelling   &   Software   26:1660-1674
945   doi:https://doi.org/10.1016/j.envsoft.2011.07.001

946 Gartner, J. E., Cannon, S. H., & Santi, P. M. (2014). Empirical models for predicting volumes of sediment
947   deposited by debris flows and sediment-laden floods in the transverse ranges of southern California.
948   Engineering Geology, 176, 45-56. doi:https://doi.org/10.1016/j.enggeo.2014.04.008

949 George, D. L., & Iverson, R. M. (2014). A depth-averaged debris flow model that includes the effects of evolving
950   dilatancy. II. Numerical predictions and experimental tests. Proceedings of the Royal Society A:
951   Mathematical, Physical and Engineering Sciences, 470(2170), 20130820. doi:10.1098/rspa.2013.0820
952 Gochis, D. J., & Chen, F. (2003). Hydrological Enhancements to the Community Noah Land Surface Model (No.
953   NCAR/TN-454+STR). University Corporation for Atmospheric Research. doi:10.5065/D60P0X00
954 Goodrich, D., Burns, I., Unkrich, C., Semmens, D., Guertin, D., Hernandez, M., . . . Levick, L. (2012).
955   KINEROS2/AGWA: model use, calibration, and validation. Transactions of the ASABE, 55, 1561-
956   1574. doi:10.13031/2013.42264
957 Goss, M., Swain, D. L., Abatzoglou, J. T., Sarhadi, A., Kolden, C. A., Williams, A. P., & Diffenbaugh, N. S.
958   (2020). Climate change is increasing the likelihood of extreme autumn wildfire conditions across
959   California. Environmental Research Letters, 15(9), 094016. doi:10.1088/1748-9326/ab83a7
960 Gregoretti, C., & Fontana, G. D. (2008). The triggering of debris flow due to channel-bed failure in some alpine
961   headwater basins of the Dolomites: analyses of critical runoff. Hydrological Processes, 22(13), 2248-
962   2263. doi:https://doi.org/10.1002/hyp.6821
963 Gupta, H. V., Kling, H., Yilmaz, K. K., & Martinez, G. F. (2009). Decomposition of the mean squared error and
964   NSE performance criteria: Implications for improving hydrological modelling. Journal of Hydrology,
965   377(1), 80-91. doi:https://doi.org/10.1016/j.jhydrol.2009.08.003
966 Handwerger, A. L., Jones, S. Y., Amatya, P., Kerner, H. R., Kirschbaum, D. B., and Huang, M.-H. (in review):
967   Strategies for landslide detection using open-access synthetic aperture radar backscatter change in
968   Google Earth Engine, Nat. Hazards Earth Syst. Sci. Discuss.
969 Huang, X., Swain, D. L., & Hall, A. D. (2020). Future precipitation increase from very high resolution ensemble
970   downscaling of extreme atmospheric river storms in California. 6(29), eaba1323.
971   doi:10.1126/sciadv.aba1323 %J Science Advances
972 Ice, G. G., Neary, D. G., & Adams, P. W. (2004). Effects of Wildfire on Soils and Watershed Processes. Journal
973   of Forestry, 102(6), 16-20. doi:10.1093/jof/102.6.16
974 Iverson, R. M., & George, D. L. (2014). A depth-averaged debris flow model that includes the effects of evolving
975   dilatancy. I. Physical basis. Proceedings of the Royal Society A: Mathematical, Physical and
976   Engineering Sciences, 470(2170), 20130819. doi:10.1098/rspa.2013.0819
977 Jolly, W. M., Cochrane, M. A., Freeborn, P. H., Holden, Z. A., Brown, T. J., Williamson, G. J., & Bowman, D.
978   M. J. S. (2015). Climate-induced variations in global wildfire danger from 1979 to 2013. Nature
979   Communications, 6(1), 7537. doi:10.1038/ncomms8537
980 Julien, P. Y., Saghafian, B., & Ogden, F. L. (1995). RASTER-BASED HYDROLOGIC MODELING OF
981   SPATIALLY-VARIED SURFACE RUNOFF1. JAWRA Journal of the American Water Resources
982   Association, 31(3), 523-536. doi:https://doi.org/10.1111/j.1752-1688.1995.tb04039.x
983 Kean, J. W., McCoy, S. W., Tucker, G. E., Staley, D. M., & Coe, J. A. (2013). Runoff-generated debris flows:
984   Observations and modeling of surge initiation, magnitude, and frequency. Journal of Geophysical
985   Research: Earth Surface, 118(4), 2190-2207. doi:https://doi.org/10.1002/jgrf.20148
986 Kean, J. W., & Staley, D. M. (2021). Forecasting the Frequency and Magnitude of Postfire Debris Flows Across
987   Southern California. Earth's Future, 9(3), e2020EF001735. doi:https://doi.org/10.1029/2020EF001735
988 Kean, J. W., Staley, D. M., & Cannon, S. H. (2011). In situ measurements of postfire debris flows in southern
989   California: Comparisons of the timing and magnitude of 24 debris flow events with rainfall and soil
990   moisture conditions. Journal of Geophysical Research F: Earth Surface, 116(4).
991   doi:10.1029/2011JF002005
992 Kinoshita, A. M., & Hogue, T. S. (2015). Increased dry season water yield in burned watersheds in Southern
993   California. Environmental Research Letters, 10(1), 014003. doi:10.1088/1748-9326/10/1/014003

994 Kling, H., Fuchs, M., & Paulin, M. (2012). Runoff conditions in the upper Danube basin under an ensemble of
995   climate change scenarios. Journal of Hydrology, 424-425, 264-277.
996   doi:https://doi.org/10.1016/j.jhydrol.2012.01.011
997 Larsen, I., MacDonald, L., Brown, E., Rough, D., Welsh, M., Pietraszek, J., . . . Schaffrath, K. (2009). Causes
998   of Postfire Runoff and Erosion: Water Repellency, Cover, or Soil Sealing? Soil Science Society of
999   America Journal - SSSAJ, 73. doi:10.2136/sssaj2007.0432
1000 Lahmers, T. M., Gupta, H., Castro, C. L., Gochis, D. J., Yates, D., Dugger, A., . . . Hazenberg, P. J. J. o. H.
1001   (2019). Enhancing the structure of the WRF-Hydro hydrologic model for semiarid environments. 20(4),
1002   691-714.
1003 Lahmers, T. M., Castro, C. L., & Hazenberg, P. (2020). Effects of Lateral Flow on the Convective Environment
1004   in a Coupled Hydrometeorological Modeling System in a Semiarid Environment, Journal of
1005   Hydrometeorology, 21(4), 615-642. Retrieved Sep 29, 2021, from
1006   https://journals.ametsoc.org/view/journals/hydr/21/4/jhm-d-19-0100.1.xml
1007 MacDonald, L. H., & Huffman, E. L. (2004). Postfire soil water repellency: Persistence and soil moisture
1008   thresholds. Soil Science Society of America Journal, 68, 1729-1734.
1009 Martin, D., & Moody, J. (2001). Comparison of Soil Infiltration Rates in Burned and Unburned Mountainous
1010   Watersheds. Hydrological Processes, 15, 2893-2903. doi:10.1002/hyp.380
1011 McGuire, L. A., Rengers, F. K., Kean, J. W., & Staley, D. M. (2017). Debris flow initiation by runoff in a
1012   recently burned basin: Is grain-by-grain sediment bulking or en masse failure to blame? Geophysical
1013   Research Letters, 44(14), 7310-7319. doi:https://doi.org/10.1002/2017GL074243
1014 McGuire, L. A., & Youberg, A. M. (2020). What drives spatial variability in rainfall intensity-duration thresholds
1015   for post-wildfire debris flows? Insights from the 2018 Buzzard Fire, NM, USA. Landslides, 17(10),
1016   2385-2399. doi:10.1007/s10346-020-01470-y
1017 McMichael, C. E., & Hope, A. S. (2007). Predicting streamflow response to fire-induced landcover change:
1018   implications of parameter uncertainty in the MIKE SHE model. J Environ Manage, 84(3), 245-256.
1019   doi:10.1016/j.jenvman.2006.06.003
1020 Meixner, T., & Wohlgemuth, P. (2003). Climate Variability, Fire, Vegetation Recovery, and Watershed
1021   Hydrology.
1022 Meyer, G. A., & Wells, S. G. (1997). Fire-related sedimentation events on alluvial fans, Yellowstone National
1023   Park, U.S.A. Journal of Sedimentary Research, 67(5), 776-791. doi:10.1306/D426863A-2B26-11D7-
1024   8648000102C1865D
1025 Mikoš, M., & Bezak, N. (2021). Debris Flow Modelling Using RAMMS Model in the Alpine Environment With
1026   Focus on the Model Parameters and Main Characteristics. 8(732). doi:10.3389/feart.2020.605061
1027 Miller, D. A., & White, R. A. (1998). A Conterminous United States Multilayer Soil Characteristics Dataset for
1028   Regional Climate and Hydrology Modeling, Earth Interactions, 2(2), 1-26. Retrieved Sep 27, 2021, from
1029   https://journals.ametsoc.org/view/journals/eint/2/2/1087-3562_1998_002_0001_acusms_2.3.co_2.xml
1030 Mitsopoulos, I. D., & Mironidis, D. (2006). Assessment of post fire debris flow potential in a Mediterranean
1031   type ecosystem. WIT Transactions on Ecology and the Environment, 90.
1032 Moody, J., & Ebel, B. (2012). Hyper-dry conditions provide new insights into the cause of extreme floods after
1033   wildfire. CATENA, 93, 58-63. doi:10.1016/j.catena.2012.01.006
1034 Moody, J., Shakesby, R., Robichaud, P., Cannon, S., & Martin, D. A. J. E.-S. R. (2013). Current research issues
1035   related to post-wildfire runoff and erosion processes. 122, 10-37.
1036 Moriasi, D. N., Arnold, J. G., Van Liew, M. W., Bingner, R. L., Harmel, R. D., & Veith, T. L. (2007). Model
1037   evaluation guidelines for systematic quantification of accuracy in watershed simulations. Transactions
1038   of the ASABE, 50(3), 885-900.

1039   Nash, J. E., & Sutcliffe, J. V. (1970). River flow forecasting through conceptual models part I — A discussion
1040   of principles. Journal of Hydrology, 10(3), 282-290. doi:https://doi.org/10.1016/0022-1694(70)90255-
1041   6

1042   Neary, D., Gottfried, G., & Ffolliott, P. (2003). Post-wildfire watershed flood responses.

1043   Nikolopoulos, E.I., Destro, E., Bhuiyan, M.A.E, Borga, M., & Anagnostou, E.N. (2018). Evaluation of predictive
1044   models for postfire debris flow occurrence in the western United States Nat Hazards Earth Syst Sci
1045   18:2331-2343 doi:10.5194/nhess-18-2331-2018

1046   Niu G-Y et al. (2011) The community Noah land surface model with multiparameterization options (Noah-MP):
1047   1. Model description and evaluation with local-scale measurements J Geophys Res Atm 116
1048   doi:https://doi.org/10.1029/2010JD015139

1049   Nyman, P., Smith, H. G., Sherwin, C. B., Langhans, C., Lane, P. N. J., & Sheridan, G. J. (2015). Predicting
1050   sediment delivery from debris flows after wildfire. Geomorphology, 250, 173-186.
1051   doi:https://doi.org/10.1016/j.geomorph.2015.08.023

1052   Oakley, N. S. (2021). A warming climate adds complexity to postfire hydrologic hazard planning. Earth's Future,
1053   9, e2021EF002149. https://doi.org/10.1029/2021EF002149

1054   Ogden, F. L. J. D. o. C., & Environmental Engineering, U. o. C., Storrs. (1997). CASC2D reference manual.

1055   Parise, M, Cannon, S.H. (2008) The effects of wildfires on erosion and debris-flow generation in Mediterranean
1056   climatic areas: a first database. Proceedings of 1st World Landslide Forum. Tokyo, Japan, pp 465–468

1057   Parise, M., & Cannon, S. H. (2009, April). A database on post-fire erosion rates and debris flows in
1058   Mediterranean-Basin watersheds. In EGU General Assembly Conference Abstracts (p. 1530).

1059   Parise, M., Cannon, S.H. (2012) Wildfire impacts on the processes that generate debris flows in burned
1060   watersheds Nat Hazards 61:217-227 doi:10.1007/s11069-011-9769-9

1061   Polade, S.D., Gershunov, A., Cayan, D.R, Dettinger, MD, & Pierce, D.W. (2017) Precipitation in a warming
1062   world: Assessing projected hydro-climate changes in California and other Mediterranean climate
1063   regions Scientific Reports 7:10783 doi:10.1038/s41598-017-11285-y

1064   Qi, Y., S. Martinaitis, J. Zhang, & S. Cocks. (2016). A real-time automated quality control of hourly rain gauge
1065   data based on multiple sensors in MRMS system. J. Hydrometeor., 17, 1675–1691,
1066   https://doi.org/10.1175/JHM-D-15-0188.1.

1067   Rengers, F. K., McGuire, L. A., Kean, J. W., Staley, D. M., & Hobley, D. E. J. (2016). Model simulations of
1068   flood and debris flow timing in steep catchments after wildfire. Water Resources Research, 52(8), 6041-
1069   6061. doi:https://doi.org/10.1002/2015WR018176

1070   Robichaud, P., Beyers, J., & Neary, D. (2000). Evaluating the effectiveness of postfire rehabilitation treatments.

1071   Rosso R, Rulli MC, Bocchiola D (2007) Transient catchment hydrology after wildfires in a Mediterranean basin:
1072   runoff, sediment and woody debris Hydrol Earth Syst Sci 11:125-140 doi:10.5194/hess-11-125-2007

1073   Rulli, M. C., & Rosso, R. (2007). Hydrologic response of upland catchments to wildfires. Advances in Water
1074   Resources, 30(10), 2072-2086. doi:https://doi.org/10.1016/j.advwatres.2006.10.012

1075   Santi, P. M., deWolfe, V. G., Higgins, J. D., Cannon, S. H., & Gartner, J. E. (2008). Sources of debris flow
1076   material in burned areas. Geomorphology, 96(3-4), 310-321. doi:10.1016/j.geomorph.2007.02.022

1077   Santi, P. M., & Morandi, L. (2013). Comparison of debris flow volumes from burned and unburned areas.
1078   Landslides, 10(6), 757-769.

1079   Schaefli, B., & Gupta, H. V. (2007). Do Nash values have value? Hydrological Processes, 21(15), 2075-2080.
1080   https://doi.org/10.1002/hyp.6825

1081   Scheip, C. M., & Wegmann, K. W. (2021). HazMapper: A global open-source natural hazard mapping
1082   application in Google Earth Engine. Natural Hazards and Earth System Sciences, 21(5), 1495-1511.

1083   Schönfelder, L., Bakken, T., Alfredsen, K., & Adera, A. (2017). Application of HYPE in Norway.

1084   Scott, D. F., & Van Wyk, D. B. (1990). The effects of wildfire on soil wettability and hydrological behaviour of
1085   an afforested catchment. 121, 239. doi:10.1016/0022-1694(90)90234-o
1086   Scott, D. J. J. o. H. (1993). The hydrological effects of fire in South African mountain catchments. 150, 409-432.
1087   Shakesby, R. A., & Doerr, S. H. (2006). Wildfire as a hydrological and geomorphological agent. Earth-Science
1088   Reviews, 74(3), 269-307. doi:https://doi.org/10.1016/j.earscirev.2005.10.006
1089   Shen H, Lynch, B., Poulsen, C.J., & Yanites, B.J. (2021) A modeling framework (WRF-Landlab) for simulating
1090   orogen-scale   climate-erosion   coupling   Computers   &   Geosciences   146:104625
1091   doi:https://doi.org/10.1016/j.cageo.2020.104625
1092   Sidman, G., Guertin, D., Goodrich, D., Unkrich, C., & Burns, I. (2016). Risk assessment of post-wildfire
1093   hydrological response in semiarid basins: the effects of varying rainfall representations in the
1094   KINEROS2/AGWA model. International Journal of Wildland Fire, 25, 268-278. doi:10.1071/WF14071
1095   Staley, D. M., Negri, J. A., Kean, J. W., Laber, J. L., Tillery, A. C., & Youberg, A. M. (2016). Updated logistic
1096   regression equations for the calculation of postfire debris flow likelihood in the western United States
1097   (2016-1106). Retrieved from Reston, VA: http://pubs.er.usgs.gov/publication/ofr20161106
1098   Stoof, C. R., Vervoort, R. W., Iwema, J., van den Elsen, E., Ferreira, A. J. D., & Ritsema, C. J. (2012).
1099   Hydrological response of a small catchment burned by experimental fire. Hydrol. Earth Syst. Sci., 16(2),
1100   267-285. doi:10.5194/hess-16-267-2012
1101   Swain, D. L. (2021). A Shorter, Sharper Rainy Season Amplifies California Wildfire Risk. Geophysical Research
1102   Letters, 48(5), e2021GL092843. doi:https://doi.org/10.1029/2021GL092843
1103   Swain, D. L., Langenbrunner, B., Neelin, J. D., & Hall, A. (2018) Increasing precipitation volatility in twenty-
1104   first-century California Nature Climate Change 8:427-433 doi:10.1038/s41558-018-0140-y
1105   Tognacca, C., Bezzola, G., & Minor, H.-E. (2000). Threshold criterion for debris flow initiation due to channel-
1106   bed failure. Paper presented at the Debris flow hazards mitigation: Mechanics, prediction and
1107   assessment.
1108   U.S. Forest Service, Burned Area Emergency Response, Dolan Postfire BAER Soil Burn Severity Map Released,
1109   October   10,   2020,   https://inciweb.nwcg.gov/photos/CALPF/2020-10-06-1821-Dolan-PostFire-
1110   BAER/related_files/pict20200910-143346-0.pdf
1111   U.S. Forest Service, Burned Area Emergency Response, Dolan Fire Burned Area Report, October 13, 2020,
1112   https://inciweb.nwcg.gov/photos/CALPF/2020-10-06-1821-Dolan-PostFire-
1113   BAER/related_files/pict20200927-132609-0.pdf
1114   U.S. Geological Survey, Postfire Debris flow Hazards: Dolan Fire (Los Padres National Forest, CA), Landslide
1115   Hazards   Program,   retrieved   September   27,   2021,   from
1116   https://landslides.usgs.gov/hazards/postfire_debrisflow/detail.php?objectid=312
1117   Vergopolan, N., Chaney, N. W., Beck, H. E., Pan, M., Sheffield, J., Chan, S., & Wood, E. F. (2020). Combining
1118   hyper-resolution land surface modeling with SMAP brightness temperatures to obtain 30-m soil
1119   moisture   estimates.   Remote   Sensing   of   Environment,   242,   111740.
1120   doi:https://doi.org/10.1016/j.rse.2020.111740
1121   Wang, J., Wang, C., Rao, V., Orr, A., Yan, E., & Kotamarthi, R. (2019). A parallel workflow implementation
1122   for PEST version 13.6 in high-performance computing for WRF-Hydro version 5.0: a case study over
1123   the midwestern United States. Geoscientific Model Development, 12(8), 3523-3539. doi:10.5194/gmd-
1124   12-3523-2019
1125   Williams, A. P., Abatzoglou, J. T., Gershunov, A., Guzman-Morales, J., Bishop, D. A., Balch, J. K., &
1126   Lettenmaier, D. P. (2019). Observed Impacts of Anthropogenic Climate Change on Wildfire in
1127   California. Earth's Future, 7(8), 892-910. doi:https://doi.org/10.1029/2019EF001210
1128   Xia, Y., Mitchell, K., Ek, M., Cosgrove, B., Sheffield, J., Luo, L., . . . Lohmann, D. (2012). Continental-scale
1129   water and energy flux analysis and validation for North American Land Data Assimilation System

1130   project phase 2 (NLDAS-2): 2. Validation of model-simulated streamflow. Journal of Geophysical
1131   Research: Atmospheres, 117(D3). doi:https://doi.org/10.1029/2011JD016051
1132 Zhang, J. et al. (2011). National Mosaic and Multi-Sensor QPE (NMQ) system: Description, results, and future
1133   plans. Bull. Amer. Meteor. Soc., 92, 1321–1338, https://doi.org/10.1175/2011BAMS-D-11-00047.1.
1134 Zhang, J., Y. Qi, C. Langston, B., Kaney, & K. Howard. (2014). A real-time algorithm for merging radar QPEs
1135   with rain gauge observations and orographic precipitation climatology. J. Hydrometeor., 15, 1794–1809,
1136   https://doi.org/10.1175/JHM-D-13-0163.1.
1137 Zhang, J. et al. (2016). Multi-Radar Multi-Sensor (MRMS) quantitative precipitation estimation: Initial
1138   operating capabilities. Bull. Amer. Meteor. Soc., 97, 621–638, https://doi.org/10.1175/BAMS-D-14-
1139   00174.1.
1140
1141